ANL-AMMT-011

Preliminary prediction of long-term aging and creep behavior of AM 316 SS

Applied Materials Division

About Argonne National Laboratory
Argonne is a U.S. Department of Energy laboratory managed by UChicago Argonne, LLC under contract DE-AC02-06CH11357. The Laboratory's main facility is outside Chicago, at 9700 South Cass Avenue, Argonne, Illinois 60439. For information about Argonne and its pioneering science and technology programs, see www.anl.gov.

DOCUMENT AVAILABILITY

Online Access: U.S. Department of Energy (DOE) reports produced after 1991 and a growing number of pre-1991 documents are available free at OSTI.GOV (http://www.osti.gov/), a service of the U.S. Dept. of Energy's Office of Scientific and Technical Information

Reports not in digital format may be purchased by the public from the National Technical Information Service (NTIS):
U.S. Department of Commerce
National Technical Information Service
5301 Shawnee Rd
Alexandria, VA 22312
www.ntis.gov
Phone: (800) 553-NTIS (6847) or (703) 605-6000
Fax: (703) 605-6900
Email: **orders@ntis.gov**

Reports not in digital format are available to DOE and DOE contractors from the Office of Scientific and Technical Information (OSTI)
U.S. Department of Energy
Office of Scientific and Technical Information
P.O. Box 62
Oak Ridge, TN 37831-0062
www.osti.gov
Phone: (865) 576-8401
Fax: (865) 576-5728
Email: **reports@osti.gov**

Disclaimer
This report was prepared as an account of work sponsored by an agency of the United States Government. Neither the United States Government nor any agency thereof, nor UChicago Argonne, LLC, nor any of their employees or officers, makes any warranty, express or implied, or assumes any legal liability or responsibility for the accuracy, completeness, or usefulness of any information, apparatus, product, or process disclosed, or represents that its use would not infringe privately owned rights. Reference herein to any specific commercial product, process, or service by trade name, trademark, manufacturer, or otherwise, does not necessarily constitute or imply its endorsement, recommendation, or favoring by the United States Government or any agency thereof. The views and opinions of document authors expressed herein do not necessarily state or reflect those of the United States Government or any agency thereof, Argonne National Laboratory, or UChicago Argonne, LLC.

ANL-AMMT-011

Preliminary prediction of long-term aging and creep behavior of AM 316 SS

---

prepared by
Tianju Chen, Argonne National Laboratory
Sagar Bhatt, Argonne National Laboratory
Hao Deng, Argonne National Laboratory
Mark C. Messner, Argonne National Laboratory
Stephanie A. Pitts, Idaho National Laboratory
Andrea M. Jokisaari, Idaho National Laboratory
K. Dang, Los Alamos National Laboratory
L. Capolungo, Los Alamos National Laboratory

Applied Materials Division

September 2023

Abstract

This report describes the development of initial mechanism models for the long term behavior of additively manufactured (AM), laser powder-bed fusion 316H stainless steel under the conditions expected in future advanced nuclear reactors. These models focus on key features of the material microstructure and response that differ from the conventionally-manufactured wrought material. Specifically, the report describes the development of models to capture the unique response of the AM material focusing on irradiation creep and swelling, the effect of internal stress, for example caused by dislocation structure, on precipitation, and the effect of the AM grain and dislocation structure on the macroscale creep and thermal aging behavior. This single mechanism models represent progress towards a complete, physics-based model for the long-term material behavior as well as elucidate key differences in the AM material behavior, when compared to the better-understood, conventionally-manufactured 316H.

Table of Contents

List of Figures

List of Tables

1 Introduction

This report describes the development of preliminary mechanism models to predict the long-term behavior of additively manufactured, Laser Powder Bed Fusion (LPBF) 316H stainless steel. These models are part of a larger effort by the Advanced Materials & Manufacturing Technologies (AMMT) program to develop physics-based models for the long-term material performance of advanced materials operating under the conditions expected in future advanced nuclear reactors. Validated physics-based models could provide better long-term predictions for material strength and reliability, when compared to current approaches, based on empirical extrapolation techniques. Replacing these empirical methods with physics-based models could therefore reduce the amount and duration of testing required to qualify a new material, accelerating the process of qualifying advanced materials for nuclear service.

Specifically, this report describes progress towards a physics-based, mechanistic model for the long term creep and thermal aging behavior of LBPF 316H. Our work focuses on developing key mechanism models for the LPBF material, targeting differences between the wrought material microstructure and material behavior and the expected AM material structure and response. This report summarizes collaborative work at Idaho National Laboratory (INL), Los Alamos National Laboratory (LANL), and Argonne National Laboratory, with each site focusing on a different material mechanism

1. Chapter 2: a preliminary model for irradiation creep and swelling, developed at INL.
2. Chapter 3: a framework accounting for the effect of internal stress on precipitation, developed at LANL.
3. Chapter 4: a preliminary model for creep and thermal aging accounting for LPBF grain and dislocation structure, developed at Argonne.

Each of these mechanism models represents progress towards developing a complete, physics-based model for the long-term material performance. Moreover, each mechanism focuses on a unique aspect of the material microstructure, when compared to wrought material. These mechanism models therefore not only contribute towards the development of a full model for the material behavior, but also help to elucidate the key differences between the wrought and AM material response.

Chapter 5 summarizes the work accomplished this fiscal year and discusses future work needed to develop a complete model for predicting the long-term behavior of LPBF 316H. In addition to continuing to improve these mechanism models, additional work is needed to integrate the mechanisms into a complete description of the material behavior and to include interactions between the different mechanisms into the final model.

2 Development of initial MOOSE-based crystal plasticity model for irradiation creep in 316 stainless steel

Although wrought 316 stainless steel has been extensively studied, predictive simulation models for the behavior of the austenitic stainless steels under irradiation creep conditions are lacking. While phenomenological models exist [2], these models are fit to limited data and often conflict with each other. For example, the Gittus [3] and Garnder [2] phenomenological models disagree about the dependence of the irradiation creep coefficient on irradiation swelling. These models cannot be extrapolated past the calibration data range, and the scarcity of experimental data further limits the use of phenomenological models. High-fidelity, mechanism-based models are required for simulations to predict material responses. Our goal is to develop a mechanistic crystal plasticity capability to assist in interpreting the scarce irradiation creep stainless steel experimental data and predict irradiation creep behavior of additively-manufactured (AM) 316 stainless steel, which has a significantly different microstructure from conventional wrought material.

To guide the mechanism selection for the initial implementation efforts, we focused on irradiation deformation mechanisms, which are active in the operating conditions of interest for Generation IV reactors [4]. At the intermediate temperatures of interest, void swelling, precipitate evolution, and irradiation creep are active. Irradiation creep depends on the behavior of dislocation networks and the interaction of those dislocations with other radiation defects, including precipitates and point defects [4]. Glide and climb are the dislocation evolution mechanisms governing those interactions [5]. Furthermore, radiation-induced swelling is a life-limiting factor for stainless-steel components at higher temperatures [6].

For these reasons, we selected dislocation glide, void swelling, and dislocation climb as focus areas for the initial efforts to implement an irradiation creep crystal plasticity model into the Multiphysics Object-Oriented Simulation Environment (MOOSE) code. Some existing crystal plasticity capabilities are available within MOOSE, including a generalized stress residual minimization scheme and an applied shear stress calculation algorithm [7]. These capabilities are demonstrated with the basic Kalidindi model [8], which is developed for a face centered cubic (FCC) crystal structure. The Kalidindi model, however, tracks only the evolution of the crystal slip system hardening rather than microstructure features, such as dislocation and defect densities, and thus is unsuited for the mechanistic focus of this work. Other models have been developed from the MOOSE code for use with body centered cubic (BCC) crystal systems, including models for material behavior prediction after radiation exposure [9, 10]. Although BCC and FCC crystals are both cubic-based systems, the slip planes and slip directions are different for each crystal system. The number of possible slip systems in BCC systems is significantly larger, particularly at higher temperatures where up to 48 slip systems can be active [11]. The larger number of slip systems in BCC materials enables dislocation motion through dislocation cross-slip, and cross-slip is a mechanism for dislocations to by-pass obstacles, including irradiation defects [12, 10]. FCC materials do not readily demonstrate cross slip and deform through other dislocation motion mechanisms. For the austenitic 316 stainless steel of interest in this work, a new, FCC-appropriate crystal plasticity model is required to capture the relevant deformation mechanisms of dislocation glide and climb. The new model should also leverage the symmetry of the FCC crystal system.

Implementing this crystal plasticity model into MOOSE will ensure easy access to the simulation capability through the open-source structure of MOOSE [13] and will enable coupling to additional codes in the near future. Open-source access to the code will allow collaborators, both internal and external, to use this capability, accelerating the ability to understand the effect of AM specific microstructures and process variability on the irradiation creep response of the material. This chapter presents the progress made in these three development areas.

2.1 Initial crystal plasticity model for stainless steel

The dislocation glide model forms the basis of the crystal plasticity capability as the fundamental dislocation movement mechanism. In selecting a suitable crystal plasticity model for implementation into MOOSE, we applied two guiding metrics: suitability for irradiation creep modeling and simulation applications and compatibility with the other mechanistic modeling development efforts in the work package. A dislocation glide model, developed initially for thermal creep in 316 stainless steel by Hu and Cocks [14], was selected for this work. This thermal creep model is being adapted for dislocation network evolution in advanced manufactured stainless steel by ANL. As a model initially developed for thermal creep, we anticipate that this formulation will be suitable for the long time frame of irradiation creep simulation needs, and it will allow for a natural transition to a thermal creep mechanism at elevated temperatures. The Hu-Cocks model uses a per-slip-plane basis as the foundation of the constitutive law formulation. Rather than tracking the dislocation densities on individual slip systems (12 systems) as other crystal plasticity formulations have done [8, 15, 16, 9, 12, 10, 17], the Hu-Cocks model tracks dislocation pinning points on each of the slip planes (4 planes). Barriers to dislocation motion, including forest dislocations, solutes, and solid precipitates are also tracked on a per-slip plane basis.

Implementing and verifying the dislocation glide model first within MOOSE ensures a solid code foundation for additional development, scientific interpretation (and re-interpretation) of experimental data, prediction of irradiation creep behavior for AM specific microstructures, and understanding the impact of AM process variability on irradiation creep response. This approach will also facilitate the future combination of thermal and irradiation creep development efforts at ANL and INL. Contributions to the crystal slip system hardening due to solutes and solid precipitates within the Hu-Cocks model will also enable future connections to the precipitation kinetics model under development by LANL. In this section, we present the details of the mathematical formulation of the Hu-Cocks dislocation glide model, show a few demonstration cases of the model implementation, and conclude with a brief summary of proposed future work.

2.1.1 Mathematical formulation and implementation

The crystal plasticity capability in MOOSE is designed to enable the development and implementation of new constitutive laws without the need to code the residual stress iteration algorithm anew [7]. As such, the constitutive Hu-Cocks dislocation glide model [14] must be adapted to an incremental formulation that tracks the applied slip system stress and slip system critical resolved shear stress on an individual slip system basis. Here the slip increment on each slip system is defined with a power law relationship as

$$\Delta\gamma^{\alpha} = \Delta\gamma_{o} \left| \frac{\tau^{\alpha}}{g^{\alpha}} \right|^{p} sign\left(\tau^{\alpha}\right) \tag{2.1}$$

where α indicates a slip system, $\Delta\gamma_o$ is the reference shear strain increment, τ^{α} is the applied shear stress on slip system α, and g^{α} is slip system α's critical resolved shear stress. The contributions to the critical resolved shear stress are

$$g^{\alpha} = g_d^{\alpha} + g_s + g_p \tag{2.2}$$

where g_d^{α} is the forest dislocation hardening, g_s is the solute strengthening, and g_p is the solid precipitate strengthening. The critical resolved shear stress can also be considered as the strength of each slip system and represents the resistance to dislocation motion. All the individual strengthening contributions follow the impenetrable barrier form and are implemented in a per-slip system manner; the superscript α indicates a slip system. The forest dislocation hardening term is calculated as a function of the pinning points per slip plane, Ω, using the relationship

$$g_d^{\alpha} = \left. \frac{\alpha_d G b}{L_d^{\Omega}} \right|_{\alpha\in\Omega} \tag{2.3}$$

where α_d is a barrier strength parameter, G is the shear modulus, b is the Burgers vector, and L_d is the mean free glide path due to forest dislocations. The contribution of the solute to the critical resolved stress is independent of the coplanar system group,

$$g_s = \frac{\alpha_s G b}{L_s}, \quad \text{where} \quad L_s = \left(\frac{1}{cb}\right)^{1/2}. \tag{2.4}$$

The barrier strength parameter is represented by α_s and c is the solute concentration [14]. Similarly, the solid precipitate strengthening contribution is also independent of coplanar system group and is computed as a function of the average precipitate radius r_p and precipitate number density N_p

$$g_p = \frac{\alpha_p G b}{r_p} \sqrt{\frac{3}{2\pi} \left(\frac{4}{3}\pi r_p^3 N_p\right)} \tag{2.5}$$

where α_p is the solid precipitate barrier strength parameter [18].

The primary state variable in the Hu-Cocks dislocation glide model is the number density of pinning points per slip plane [14]. The dislocation mean free path value, as used in the dislocation forest hardening expression Equation 2.3, is related to the pinning point number density

$$N_d = \frac{1}{(L_d)^2}. \tag{2.6}$$

The evolution of the pinning point number density is defined on each slip plane, Ω, and defined as a function of the coplanar slip system groups. The pinning point number density is incremented in the usual fashion

$$N_d^{\Omega} = \Delta N_d^{\Omega} + N_{do}. \tag{2.7}$$

Correspondingly, the pinning point density increment is defined in a per slip plane, or per coplanar group, basis, as the sum of the self plane and latent plane evolution,

$$\Delta N_d^{\Omega} = \Delta N_{self}^{\Omega} + \Delta N_{latent}^{\Omega}. \tag{2.8}$$

From Hu and Cocks [14, 18], the pinning point evolution due to interaction on the self slip plane Ω is defined as

$$\Delta N_{self}^{\Omega} = \frac{j_s}{s} \Delta\gamma^{\Omega} \tag{2.9}$$

and the pinning point density evolution due to latent planes contribution is defined as

$$\Delta N_{latent}^{\Omega} = \sum_{\omega \neq \Omega} \frac{j}{s} \frac{1}{(m-1)} \Delta\gamma^{\omega} \tag{2.10}$$

where m is the number of slip planes and is defined as four for FCC crystals. The coefficient ratio j_s/s is the combined self-hardening coefficient and j/s is the latent hardening combined coefficient ratio. [14]. The shear strain increment $\Delta\gamma^{\Omega}$ on each slip plane Ω is the sum of the shear strain increments on all of the active coplanar slip systems that share plane Ω

$$\Delta\gamma^{\Omega} = \sum_{\alpha \in \Omega} \Delta\gamma^{\alpha}. \tag{2.11}$$

The updated pinning point number density is then used to compute the forest dislocation hardening contribution. Substituting Equation 2.6, the relationship between pinning point density and the dislocation mean free path, into Equation 2.3, the forest hardening expression can be rewritten in terms of the pinning point density

$$g_d^{\alpha} = \alpha_d G b \sqrt{N_d^{\Omega}}\Big|_{\alpha \in \Omega} \tag{2.12}$$

Because the pinning points are computed on a per plane basis while the slip resistance is computed on a per slip system basis, the forest hardening calculation will use the same value of N_d^{Ω} for all slip systems α that share the slip plane Ω.

2.1.2 Demonstration examples

The implementation of the Hu-Cocks dislocation glide crystal plasticity model is demonstrated with a simulation in which the solid precipitate radius and number density variation are prescribed. The single stainless steel crystal is loaded in tension along the [001] crystallographic direction, which is aligned with the z-axis of the simulation domain, with a traction boundary condition corresponding to 175 MPa applied to the front surface, along the [001] crystallographic direction. Pinned displacement boundary conditions are applied to the back surface of crystal, such that the crystal is allowed to contract along the x- and y-axes, in the [100] and [010] crystallographic directions, respectively. Elastic constants for 316 stainless steel and parameters from the original model publications are used [14, 18].

As seen in Figure 2.1, the prescribed smaller precipitate radius and lower number density lowered the crystal slip system strength via the physics contained in Equations 2.2 and

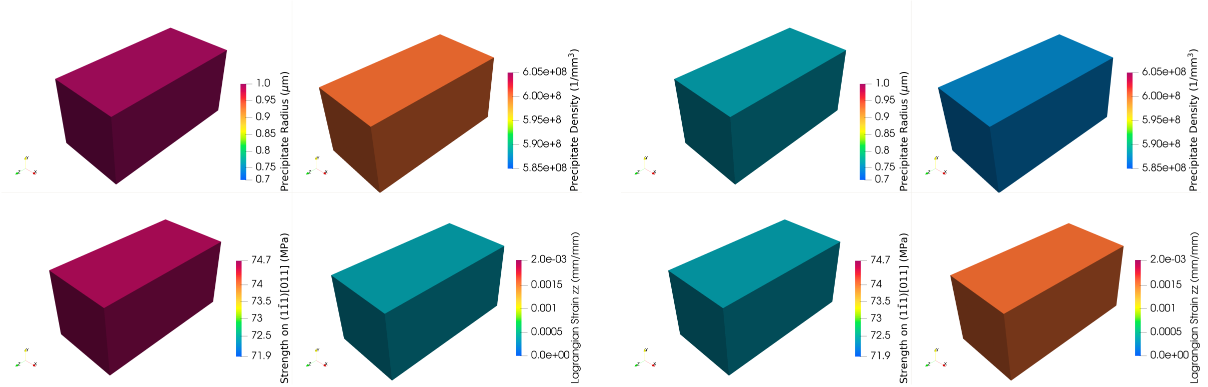

(a) Larger precipitate radius, number density (b) Smaller precipitate radius, number density

Figure 2.1: This demonstration simulation shows the expected lowering of a representative crystal slip system strength in response to prescribed reductions in the precipitate radius (from 1.0 μm to 0.77μm) and number density (from 6e-8 1/mm^3 to 5.87e-8 1/mm^3). Under a tensile load applied in the [001] direction, the Lagrangian strain value, zz-component, increases in response to the lower precipitate hardening contribution. The [100] and [010] crystallographic directions are aligned with the x- and y-axes, respectively.

2.5. The reduced slip system strength lowers the barrier to dislocation motion, resulting in additional dislocation glide and plastic deformation. As expected, the Lagrangian strain component in the loading direction increases in response to the reduced slip system strength from Figure 2.1a to Figure 2.1b, while the applied tensile traction load remains constant.

A set of verification cases was also performed with the implemented Hu-Cocks dislocation glide model. As in the demonstration case, Figure 2.1, a single crystal in a short bar geometry was pinned on the back z-plane (normal to the negative z-axis direction) and loaded with a surface traction applied to the front z-plane; the applied tensile stress load was along the positive z-axis. Elastic constants for wrought 316 stainless steel and crystal plasticity parameters from the original model publications [14, 18] were also used in these simulations. To verify the stress response trends of the dislocation glide model, three separate crystallographic orientations were simulated: [111], [110], and [001]. Three different stress loading rates were also applied: 25, 35, and 45 MPa/s, for the first 10 seconds of the simulations. After the initial loading ramp, the applied stress load was held constant at a terminal value of 250, 350, and 450 MPa, respectively.

The expected trends of a higher yield stress for the [111] loading orientation, compared to the [110] and the [001] orientations, are clearly demonstrated in Figure 2.2. Because these loading rates are high, many of the simulations did not reach the terminal stress load value. These simulations did, however, demonstrate plastic deformation. In Figure 2.2a, only elastic deformation is observed in the [111] orientation curve because the yield stress for the [111] orientation is above the 250 MPa terminal load value for this case. Numerical convergence issues significantly impacted the simulation run time once plastic deformation begins. Addressing the source of these run time challenges is a key focus in the near-term future.

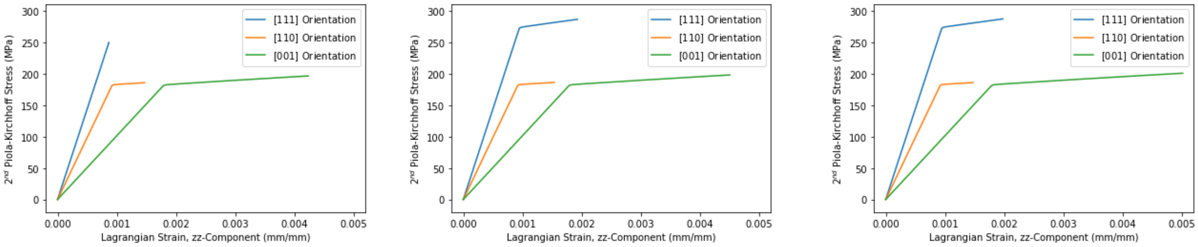

(a) Applied 25 MPa/s Ramp (b) Applied 35 MPa/s Ramp (c) Applied 45 MPa/s Ramp

Figure 2.2: Results from verification cases under three different tensile load ramp conditions. Variations in loading orientations demonstrate the expected stress response trends from the Hu-Cocks dislocation glide model: the [111] loading orientation yield stress is larger than the yield stress of the [110] and the [001] loading orientations.

2.1.3 Future work

Submission of this implemented Hu-Cocks crystal plasticity model to the MOOSE repository [13] is planned as near-term future work. The dislocation glide crystal plasticity model will also be extended to connect to the volumetric eigenstrain for irradiation swelling, Section 2.2, and a dislocation climb model, Section 2.3, linking together multiple physical processes for irradiation creep. Continued development to extend the approach for incorporating hardening due to solutes and precipitates while these features undergo evolution is another potential future work focus, in collaboration with efforts led by LANL.

2.2 Irradiation swelling eigenstrain model

The formation and evolution of voids in an irradiated material produces a volume change, known as irradiation swelling, and this phenomenon occurs in materials at intermediate temperatures when exposed to radiation doses [4]. Void growth can be thought of the incorporation of free volume outside of the material into the material itself by defect transport mechanisms. For a void to grow, atoms that were within the volume enclosed by the void are transported away from the void and generally are transported to sinks such as surfaces and grain boundaries [2]. While much research has been devoted to predicting void evolution [19] and swelling behavior of the material [4], high-fidelity predictions of the impact of void swelling on the crystal mechanical response has not been as fully explored. The influence of void swelling is known to impact the mechanical properties of irradiated materials; the impact on the mechanical behavior increases with additional irradiation swelling [6]. The volume change due to void evolution can be represented as an isotropic volumetric eigenstrain. This eigenstrain in turn elicits a stress response, which may produce plastic deformation and history dependence in a metallic crystal material, such as stainless steel.

This section presents an overview of the volumetric eigenstrain implemented in the MOOSE crystal plasticity capability, followed by a series of verification cases, and concludes with a summary of proposed future work to couple this eigenstrain model to a cluster dynamics framework.

2.2.1 *Mathematical formulation and implementation*

The volumetric eigenstrain imposed on the material due to voids is calculated as a function of the void volume. In this initial implementation, we assume the voids are spherical and the void characteristics, radius and number density, are uniform at a finite element method integration point. The volume change due to voids is given as

$$\frac{\Delta V}{V_o} = \frac{4\pi}{3} r^3 \rho_v \tag{2.13}$$

where r is the void radius and ρ_v is the number density [19]. Consistent with the crystal plasticity implementation described above, we assume units of mm and 1/mm^3 for the radius and number density, respectively. The volumetric strain is converted to an equivalent linear measure following the well-accepted practice of taking the cubic root. The current equivalent linear strain increment is calculated as the difference between the current linear measure and the linear measure from the previous time step. That increment is multiplied by the Rank-2 identity tensor to calculate the linear expansion tensor,

$$\Delta \boldsymbol{\epsilon}^v = \mathbf{I} \cdot \Delta l = \mathbf{I} \cdot \left[\left(\frac{\Delta V}{V_o} \bigg|_t \right)^{1/3} - \left(\frac{\Delta V}{V_o} \bigg|_{(t-1)} \right)^{1/3} \right]. \tag{2.14}$$

The volumetric eigenstrain is incorporated into the MOOSE crystal plasticity framework through the multiplicative decomposition of the deformation gradient tensor,

$$\mathbf{F}^T = \mathbf{F}^e \mathbf{F}^P \mathbf{F}^v \tag{2.15}$$

where the superscripts T, e, P, and v indicate the total, elastic, plastic, and volumetric deformation gradients, respectively [20, 21]. The volumetric deformation gradient is calculated as a function of the linear expansion tensor, Equation 2.14, which is first rotated into the local crystal orientation:

$$\mathbf{F}^v = \left(\boldsymbol{\epsilon}_v^R \right)^{-1} \mathbf{F}_{old}^v \qquad \text{where} \qquad \boldsymbol{\epsilon}_v^R = \mathbf{I} - \Delta \boldsymbol{\epsilon}^v \mathbf{R} \tag{2.16}$$

where $\mathbf{F}_{old}^v$ is the volumetric deformation from the previous time step and $\mathbf{R}$ is the rotation tensor defined by the crystal orientation Euler angles. Finally, the Lagrangian eigenstrain is defined as a function of the volumetric deformation gradient, following the approach defined for thermal eigenstrains in a crystal plasticity formation [22]:

$$\mathbf{E}^v = \frac{1}{2} \left((\mathbf{F}^v)^T \mathbf{F}^v - \mathbf{I} \right). \tag{2.17}$$

The use of the deformation gradient in the eigenstrain calculation ensures the material history dependence is retained. Maintaining this history dependence enables the coupled crystal plasticity model to respond to the applied eigenstrain with both an immediate stress increase and a longer-term stress relaxation response.

2.2.2 Verification cases

The volumetric eigenstrain model for void swelling was tested with a series of simple verification cases. The results of these verification simulations demonstrate the computed eigenstrain and stress response are in agreement with the expected behavior. These verification simulations considered a 1 mm^3 single crystal cube. The [100], [010], and [001] crystallographic directions are aligned with the x-, y-, and z-axes, respectively. Displacement boundary conditions were applied such that the crystal was constrained in the z-direction and allowed to expand in the x- and y-directions in response to the applied eigenstrain. Void number density and radius evolution were connected to the applied temperature, which was increased at a rate of 10^oC/min and then held constant, see Figure 2.3.

The simpler Kalidindi crystal plasticity model for FCC materials [8] was used in these verification simulations, in place of the Hu-Cocks model described above. Elastic constants for 316 stainless steel are used in these simulations, without temperature dependence, to isolate the stress response sensitivity to the applied eigenstrain.

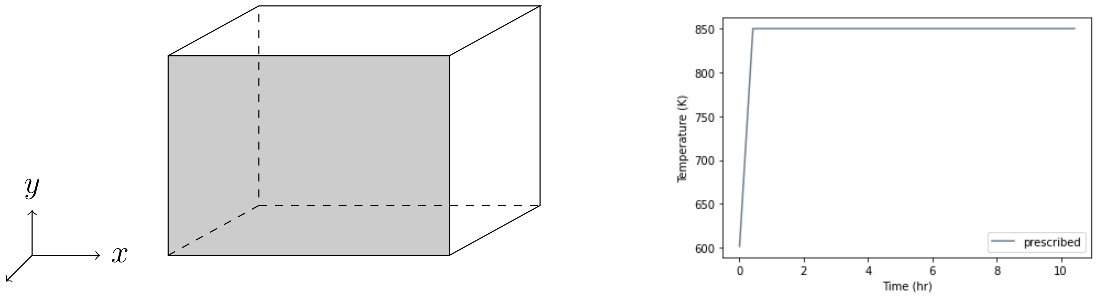

Figure 2.3: Constraints applied in the verification simulations included pinned displacement boundary conditions applied on the front z-direction face shown in grey (left) and applied temperature profile (right).

Only the void characteristics change with temperature in these simulations, and a uniform void distribution is maintained throughout the material cube. The prescribed variation of the void number density and radius for the series of verification cases is shown in Figure 2.4; the last case, Figure 2.4e, is loosely based on data collected for the average void diameter and total volume fraction in 316 stainless steel under varying neutron doses and temperatures [1].

Each verification begins with an extreme void number density value to show the effect of the introduced eigenstrain; in all cases but Figure 2.4c, this initial void number density value is zero.

The calculated linear expansion strain and void eigenstrain vary during the prescribed temperature ramp (the first 25 minutes in the simulation). After the temperature ramp, when the void characteristics are held constant, the linear expansion and eigenstrain measures also remain constant. In Figure 2.5, the evolution of these two strain measures is only shown over the course of the temperature ramp. Because the temperature ramp is constant, see Figure 2.3, temperature is used as a proxy for time in these plots.

We note the history-dependence in the eigenstrain calculation: the difference between the linear expansion strain and the eigenstrain evolution is clearest in Figures 2.5b, 2.5d, and

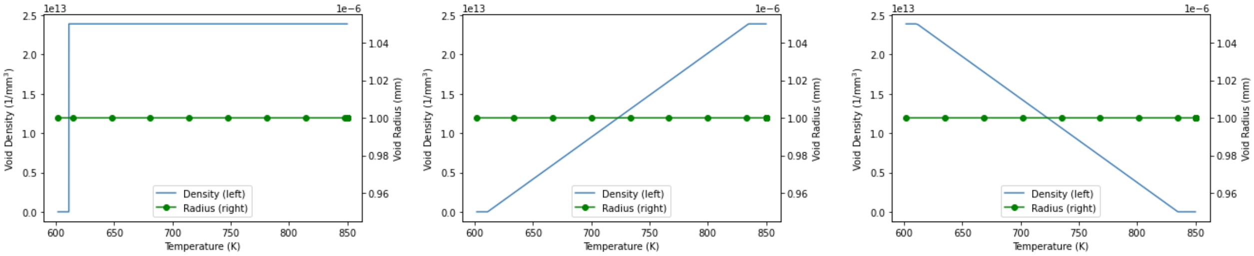

(a) Constant void density (b) Linearly increasing density (c) Linearly decreasing density

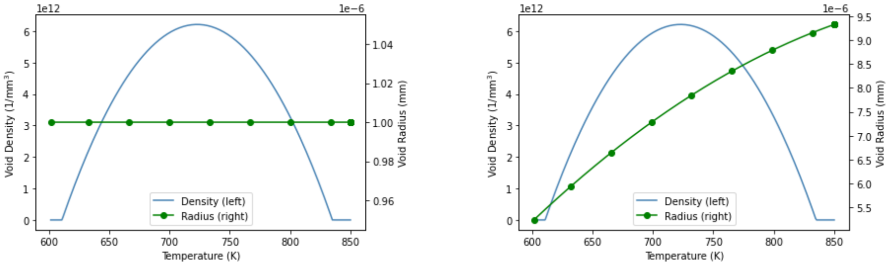

(d) Parabolic void number density (e) Representative density, radius

Figure 2.4: Prescribed void number density and radius evolution for the void swelling eigenstrain verification cases, increasing in complexity. The fifth case (e) is loosely based on data from [1].

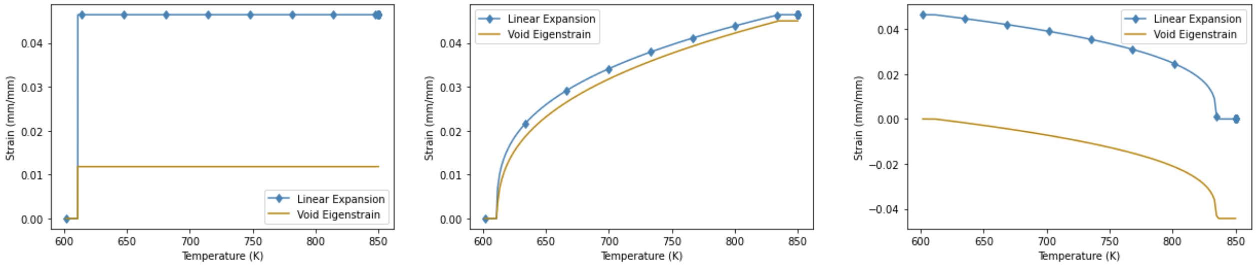

(a) Constant number density (b) Linearly increasing density (c) Linearly decreasing density

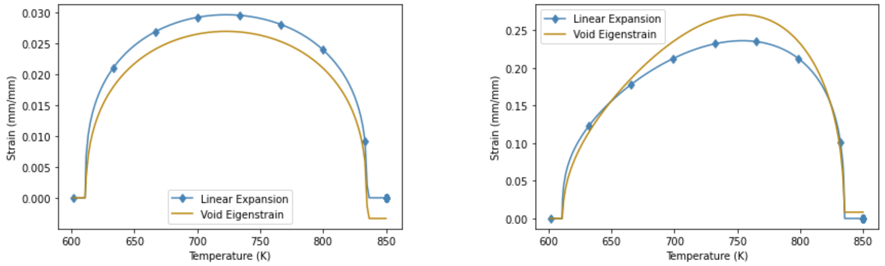

(d) Parabolic void number density (e) Representative density, radius

Figure 2.5: Evolution of the state-independent linear expansion strain (blue curves with markers) and history-dependent void swelling eigenstrain (yellow curve, no markers) with temperature for the five verification cases.

2.5e. While the linear expansion strain is only a function of the void state, Equation 2.14, the dependence on the previous time step deformation gradient, Equations 2.16 and 2.17, introduces a state dependence into the eigenstrain. The incomplete recovery of the eigenstrain state, Figures 2.5d and 2.5e in particular, demonstrate the influence of plastic slip history from the coupled crystal plasticity model.

The long-term stress response to the induced void swelling eigenstrain is of interest for irradiation creep modeling applications. To investigate the influence of the history-dependent void eigenstrain on the crystal plasticity stress response, we continued the simulated hold period of 10 hours after the temperature ramp, Figure 2.3. In Figure 2.6, the second Piola-Kirchhoff stress in the constrained (z-axis) direction is plotted over a simulation period of 10.5 hours. The eigenstrain due to the voids is shown immediately below the stress response for reference.

The initial stress response in Figure 2.6 reflects the compressive or tensile stress state imposed by the eigenstrain. A tensile stress corresponds to a reduction in the applied eigenstrain, see Figure 2.6c. After the eigenstrain ceases to evolve, at approximately 0.4 hours, an immediate decay in the stress response occurs in all five cases. Notably, all of the verification cases demonstrate a nonzero steady-state stress response. The plastic deformation induced by the void swelling eigenstrain impacts the material stress state over creep-regime time frames, even after the swelling eigenstrain itself is no longer evolving. We conclude that it is necessary to include a history-dependent eigenstrain model for irradiation void swelling in simulations of stainless steel under irradiation creep conditions to better capture the stress state experienced by the material.

2.2.3 Future work

Development efforts will be completed in the near-term future to finalize the coupling between the void swelling eigenstrain model and the Hu-Cocks dislocation glide model, Section 2.1. The next development steps for the void eigenstrain model will focus on improvements to the void characteristic evolution descriptions. Future capabilities need to couple the MOOSE-based crystal plasticity model described here to a cluster dynamics code to enable more realistic void evolution and distribution predictions as well as dislocation loop populations. The crystal plasticity eigenstrain model will be extended to allow for a variety of void states in future development work. Future work may also include incorporating the role of local pressure, within the radiation defect bubbles, on the material stress state, in addition to the volume change model implemented here.

2.3 Dislocation climb model for irradiation creep

For constant stresses below the material yield strength and temperatures above 30% of the homogeneous melting temperature, steady-state creep in a crystalline metal occurs through dislocation climb by lattice diffusion and dislocation core (pipe) diffusion [5]. The dominant dislocation climb mechanism in austenitic stainless steel is core diffusion [23]. When the glide path of a dislocation is blocked by an obstacle in the slip plane, dislocation climb is one of the mechanisms used to relieve stress. Dislocation climb is a non-conservative dislocation motion in which the dislocation moves out, or climbs out, of the glide slip plane. Climb is mediated by the diffusion of point defects near the dislocation core such that the dislocation moves by increments of an atom spacing away from its original slip plane [11]. The velocity

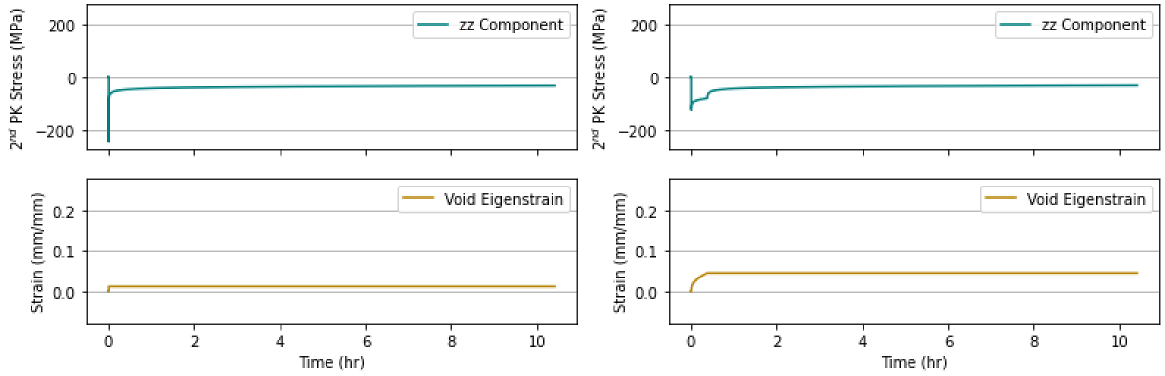

(a) Constant void number density

(b) Linearly increasing void density

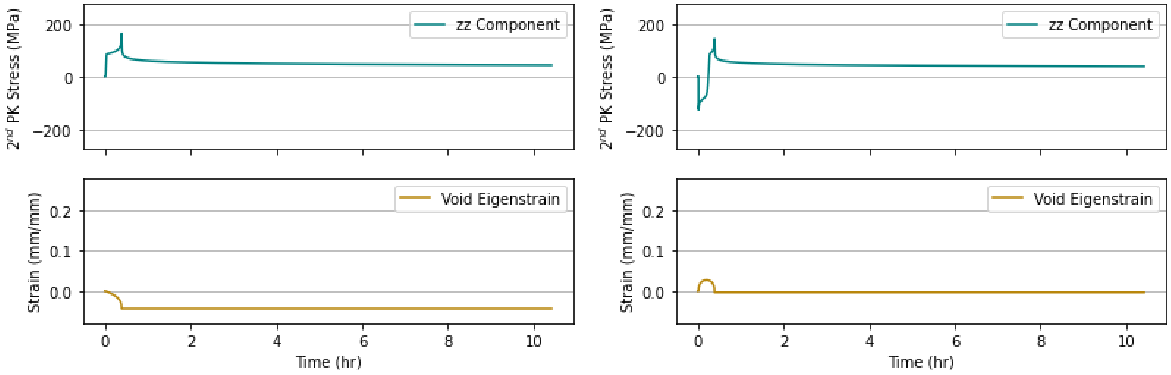

(c) Linearly decreasing void density

(d) Parabolic void number density

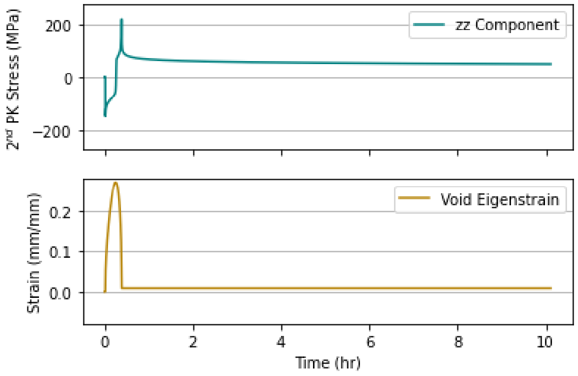

(e) Representative density, radius variation

Figure 2.6: The stress response of the crystal plasticity model in the constrained direction (zz-component) demonstrated two stages: an immediate response to the void eigenstrain and longer-term steady-state behavior after the eigenstrain is no longer evolving. The corresponding component of the void eigenstrain is shown on the same timescale for reference in each verification case. The nonzero steady-state stress response in all five verification cases demonstrates the impact of the eigenstrain in irradiation creep applications.

of dislocation climb is related to the time required for a dislocation to move sufficiently above (or below) the obstacle that dislocation glide is once again possible [5]. Because of the point defects created by atom displacement during radiation exposure, irradiation creep is less dependent on temperature than thermal creep [5].

To model dislocation climb, the climb velocity is related to the flux of interstitial and vacancy defects around the dislocation core [5]. Varying assumptions are made to simplify or expand the relationship between the point defect flux and the constitutive dislocation climb law. This section discusses the potential impact these simplifying assumptions may have on the applicability of a dislocation climb model to irradiation creep conditions and outline planned future work for the implementation of a dislocation climb model.

2.3.1 Mathematical formulation

Existing crystal plasticity formulations have employed an additive decomposition of the shear rate to account for both dislocation glide and climb activation:

$$\dot{\gamma}_{Total} = \dot{\gamma}_{glide} + \dot{\gamma}_{climb}. \tag{2.18}$$

Some crystal plasticity formulations have defined specific dislocation climb densities that evolve through an Orowan relationship with a dislocation climb velocity [15, 17]. Other models have focused on simpler recovery-type formulations [24].

The Hu-Cocks stainless steel crystal plasticity model has been extended through the minimization of the variational energy to include a dislocation climb recovery term [25, 26]:

$$\dot{L}^{\Omega}_{d-climb} = \frac{W_c D_c G b^5}{kT} \frac{1}{(L^{\Omega}_{d})^3} \tag{2.19}$$

where L^{Ω}_{d} is the mean free glide path between forest dislocations, see Equation 2.6, W_c is a fitting parameter, D_c is the core diffusivity, k is the Boltzmann constant, and T is the temperature. We note the role of the fitting parameters in Equation 2.19, which are used to replace the point defect flux through the dislocation core [25]. The simplified model formulation does offer advantages in reduced computational load. The removal of the explicit connection between the point defect flux and the dislocation climb model raises some concerns about the applicability of this particular expression to irradiation creep applications. Under irradiation conditions, maintaining the sensitivity of the dislocation climb model to evolving point defect population is important.

2.3.2 Future work

Additional work is required to reconcile the coplanar pinning point recovery approach of Hu and Cocks with a more direct connection to the point defect population in the stainless steel crystal. Such a connection would enable simulations that capture the response of creep behavior to point defect populations evolving under irradiation conditions. This goal could be accomplished with coupling to a cluster dynamics code, as has been discussed previously in Section 2.2.

Once an appropriate dislocation climb relationship has been derived, the model will be implemented into MOOSE. A similar verification procedure to that discussed in previous sections of this report will be completed before the model is submitted to the open-source MOOSE repository [13].

2.4 Conclusions

The three mechanistic-based models presented here form the initial development results towards a crystal plasticity model for irradiation creep in 316 stainless steel. These mechanisms were selected for model development because of their role in the behavior of the austenitic stainless steel under irradiation. The ability to couple the crystal plasticity model developed here with additional model developments in other work packages and to other codes will expand the number of mechanisms affecting irradiation creep that are considered in the simulations. The proposed coupling between the MOOSE-based crystal plasticity model and a cluster dynamics code will improve the irradiation creep simulations through more physically-based predictions of the irradiation point defect and void evolution.

The work presented here provides the basis of understanding irradiation creep in AM 316 stainless steel. Determination of irradiation creep mechanisms is still an area of active research, and this work will impact the scientific field of radiation effects in materials. In addition, future work will incorporate the effect of unique microstructure features in the material, resulting from additive manufacturing. Additive manufacturing frequently creates complex grain structures, such as elongated columnar grains and dislocation cell structures within individual grains. In addition, AM materials are subject to process variation that can result in different grain structures, dislocation cell sizes, and contaminates, such as oxygen, that can form fine precipitate structures through the material. Irradiation creep is dependent upon the microstructure of the material, including how the density of dislocations affect creep rate and creep rate evolution. This model development and implementation will enable prediction of irradiation creep behavior with this unique microstructure, and by extension, the modeling capability will provide for an understanding of the effect of additive manufacturing process variation on irradiation creep. Understanding the impact of process variation, microstructure variation, and thereby irradiation creep properties, is vital for rapid qualification of materials for deployment.

3 Initial framework development for precipitate nucleation in AM 316H

3.1 Introduction

Austenitic stainless steels (SS) such as 316 SS are important structural materials for nuclear applications due to their great combination of mechanical strength, ductility, and corrosion resistance. Recent advances in additive manufacturing (AM) techniques such as laser powder bed fusion (LPBF) provides new solutions to design and manufacture components with rapid and more cost-effective processing cycle as well as flexible geometry. Importantly, compared to conventionally made steels, LPBF 316 SS materials has great combination of strength and ductility at room temperature[27]. The improved mechanical properties have been attributed to grain boundary strengthening due to fine dislocation cell structures with solute micro-segregation uniquely formed during AM processes [28]. Most hypotheses and theories about the formation of these crystallographic defects point to the role of complex local stress states and rapid local heating and cooling cycles [29]. Together, these conditions can lead to particularly complex defect networks of dislocations and heterogenous distributions of precipitates. These can significantly influence the mechanical performance of the LPBF 316 SS components.

Establishing a rapid qualification framework for LPBF 316 SS is one of the key focuses of the DOE-NE Advanced Materials and Manufacturing Technologies (AMMT) program. Over the past year, the program has supported the development of mechanistic models of creep and aging for time extrapolation in LPBF 316 SS. The current framework however does not yet integrate the role of precipitation on mechanical performance. Further, state-of-the-art approach for precipitate nucleation utilizes the classical nucleation theory and regular solid solutions for complex alloys (i.e. commercial software such as TC-PRISMA and MatCalc) which is agnostic to internal and externally applied mechanical loads. Therefore, while successful in capturing the effects of chemical composition and temperature on nucleation kinetics and driving forces, simple nucleation models cannot comprehensively capture the effects of local stresses on the nucleation process. Specifically, previous approaches rely on experimental data to quantify a “correctional” pressure-dependence energy which is added to the total free energy of the system. This would underestimate/overestimate the nucleation rate of precipitates; thus preventing the model from precisely capturing the evolution of the micro-structure.

We further note that as a consequence of the build process, AMed metals will exhibit internal stress that vastly differ from conventionally made materials. Thus precipitation kinetics as well as fingerprint of precipitates are expected to be dissimilar from those in conventionally made metals. Unfortunately, to date there is no model can capture those effects.

In this past fiscal years, focus was placed on developing a new nucleation model to systematically quantify the effects of local stress on the (i) activation barrier for precipitation nucleation and (ii) the critical size of unstable nuclei. The framework is applied to the case of stainless steel (SS) 316. A first demonstration is brought to the case of a model Fe-Cr precipitate.

This report presents (i) a brief review of existing/classical precipitate nucleation models, (ii) a new nucleation model (formulation and implementation), and (iii) a comparison between the new stress-sensitive nucleation model and predictions from classical nucleation theory.

3.2 Review of existing precipitate nucleation models

Over the years, many tools with resolution ranging from the atomistic scale all the way to macroscopic length scales have been proposed to model precipitation in alloys. Atomistic approaches and methods such as Kinetic Monte Carlo (KMC) provide atomic resolution information about the mechanisms and associated driving forces for nucleation to occur. However, due to their cost, they cannot embed the effects of long-ranged mechancial fields on precipitation. Cluster dynamics approaches propose to coarse grain information gathered at the atomistic lengths scalel; they are thus promising methods to fully comprehend concurrent precipitation. However, absent a rigorous treatment of the effects of stresses on the capture efficiency, one cannot predict how internal stress will affect precipitation kinetics. Moreover, these approaches are currently not compatible with thermodynamics database such as CALPHAD (CALculation of PHAse Diagram) that contain essential information for multicomponent material systems. On the other hand, mesoscale and macroscale techniques such as phase field (PF) and Langer–Schwartz–Kampmann–Wagner (LSKW) can be coupled with CALPHAD database to determine the comprehensive process from nucleation, growth, and coarsening. These models require nucleation laws that can describe the nucleation rate of stable nucleii as a function of temperature, nominal and precipitate compositions, as well as pressures. Specifically, the common approach for precipitate nucleation commercial packages such as TC-PRISMA utilizes the classical nucleation theory (CNT) and regular solid solutions for complex alloys [30]. The following paragraph briefly discusses the nucleation model implemented in TC-PRISMA.

3.2.1 Overview of the nucleation model implemented in TC-PRISMA

The first assumption of the CNT model is that the system can be partitioned into a one-dimensional 1D Markov chain characterized by the size n of the largest droplet [31]. Based on this assumption, the steady-state nucleation rate (J_s) can be determined via the solution of the Markov chain:

$$J_s = Z\beta^* N_o \exp\left(-\frac{\Delta G^*}{kT}\right) \tag{3.1}$$

with:

$$Z = \left(\frac{\eta}{2\pi k_B T}\right) \tag{3.2}$$

$$\eta = - \left.\frac{\partial^2 \Delta G(r)}{\partial n^2}\right|_{r=r^*} \tag{3.3}$$

where Z is the Zeldovich factor, which captures the effects of the curvatures of the free-energy barrier; N_0 is the number of nucleation sites per unit volume; r is the nucleus radius, β^* is the atomic attachment rate of atoms to the critical nucleus; k_B is the Boltzmann's constant; and T is the temperature of the system. ΔG^* is nucleation energy barrier, which is the Gibbs free energy to form a critical nucleus with size r^*. The second assumption of the CNT model is that even at micro/nano -scale, the free energy can be written as the competition between the bulk and the interfacial free energies:

$$\Delta G = \frac{4}{3}\pi r^3 \Delta g_{chem} + 4\pi r^2 \gamma \tag{3.4}$$

where g_{chem} is the difference in chemical free energy between the nucleus and the matrix, γ is the surface tension of the interface between the nucleus and the surrounding matrix, which often time assume to be the interfacial energy. The first term describes a volumetric term associated with difference in the chemical energy of atoms vis a vis a reference bulk where the nucleus is assumed to be spherical with a radius r. The second term captures the additional energy penalty due to the surfaces generated between the nucleus and the surrounding matrix. With this expression, one can solve for the critical radius of the nucleus by solving this system of equations:

$$\begin{cases} \left.\frac{\partial(\Delta \mathrm{G})}{\partial r}\right|_{r=r^*} = 0 \\ \left.\frac{\partial^2(\Delta \mathrm{G})}{\partial r^2}\right|_{r=r^*} < 0 \end{cases} \tag{3.5}$$

These define an equilibrium and stable configuration. This gives the critical radius and corresponding nucleation energy barrier:

$$r_c = \frac{2\gamma}{\Delta g_{chem}} \tag{3.6}$$

$$\Delta G^* = \frac{16\pi\gamma^3}{3\Delta {g_{chem}}^2} \tag{3.7}$$

For a binary systems of α (matrix) and β (precipitate) where each phase can contain up to k elements, the atomic attachment rate can be determined via:

$$\beta^* = \frac{4\pi(r^*)^2}{a^4}\left[\sum_{i=1}^{k} \frac{\left(x_i^{\beta/\alpha} - x_i^{\alpha/\beta}\right)^2}{x_i^{\alpha/\beta} D_i}\right] \tag{3.8}$$

where $x_i^{\beta/\alpha}$ and $x_i^{\alpha/\beta}$ is the mole fraction of component i^{th} at the interface in the precipitate and matrix, respectively; D_i is the diffusion coefficient of element i^{th} in the matrix. With Eqs. 3.6-3.8, the steady-state nucleation rate can be determined using Eq. 3.1. Moreover, the time-dependent nucleation rate can also be determined using:

$$J(t) = J_s \exp\frac{-\tau}{t} \tag{3.9}$$

where t is the time and τ is the incubation time for the nucleation which is given by:

$$\tau = \frac{1}{4\pi\beta^* Z^2} \tag{3.10}$$

3.2.2 Limitations of current nucleation model

While the current nucleation model implemented in TC-PRISMA can utilize the comprehensive CALPHAD thermodynamics database for multicomponent material systems, it lacks consideration for the effects of local stress on the precipitate nucleation process due to CNT assumption. Specifically, as shown in Eq.(4) for CNT, there is no explicit term which accounts for the effects of applied stress on the Gibbs free energy of the system. One of the most common approaches to overcome this is to include the "correctional" pressure-dependence energy to ΔE_{chem} by fitting to experimental data [32]. This approach is purely empirical and would require refitting the "correctional" energy term for each new alloy system. Importantly, this approach only accounts for the effects of hydrostatic pressure and completely disregard the effects of deviatoric stresses, which have been shown to greatly influence the precipitate nucleation process [33] in SS. Another approach is to add a third energy term to Eq.(4) which corresponds to the elastic strain and misfit strain energy (related to the difference in density and elastic stiffness between the matrix and the precipitate) [34]. The implementation of this approach is often simplified by utilizing the previous derivations for the strain energies without a comprehensive micromechanics and thermodynamics treatment. In the following section, a comprehensive overview of developed nucleation model that is sensitive to the effects of local stress on both (1) the elastic strain energy (related to the phase and local composition) and (2) the transformation strain energy (related to the eigenstrain required for the formation of the precipitates) is provided.

Another drawback of the TC-PRISMA nucleation model is that the chemical driving force (Δg_{chem}) is calculated based on the assumption that the volume of the nucleus is much smaller than the volume of the matrix [30]. Specifically, the nucleus' composition and corresponding Δg_{chem} for a binary alloy can be determined via the parallel tangent line constructions. With this set-up, we get the maximum driving force for precipitation, and the composition of the nucleus is fixed for a certain supersaturation

$$\Delta g_{chem} = \sum_{i=1}^{k} x_i^{\beta} \left[\mu_i^{\alpha} \left(x_i^0 \right) - {\mu_i}^{\beta} \left(x_i^{\beta} \right) \right] \tag{3.11}$$

where μ_i^{α} and μ_i^{β} are the chemical potentials of element i^{th} in the matrix and precipitate, respectively. x_i^0 and x_i^{β} are the mole fraction of element i^{th} in the matrix and precipitate, respectively. The mole fraction in the matrix is assumed to be the original mole fraction (associated with the nominal concentration) regardless of the size of nucleus to avoid the complication in numerical approach. The overall assumption here is that the volume of the nucleus is much smaller than the volume of the matrix. In this work, a new numerical approach is developed to determine the mole fractions in both the matrix and precipitate for the ranges of nucleus and matrix sizes.

3.3 Nucleation model sensitive to local stress

To understand the role of stresses on precipitate nucleation, the configuration shown in Fig. 3.1 is shown where a precipitate nucleus is formed within the matrix under an applied stress. Chemically, the system is assumed to be binary with two elements (A and B) and two stable phases (α and β), where α is a A-rich phase and β is a B-rich phase. The system contains N moles and the precipitate contains ΔN moles. x_A^α and x_A^β are the mole fractions of component A in the matrix and precipitate, respectively. Here, the nucleus is assumed to be a sphere with radius R, which is consistent with CNT framework. R can be related to ΔN by $\Delta N = \frac{\frac{4}{3}\pi R^3}{V_m^\beta}$, where V_m^β is the molar volume of the precipitate. These choices simplify the analysis but do not limit the framework as it can be expanded to multi-component systems with more complex precipitate shape and geometry.

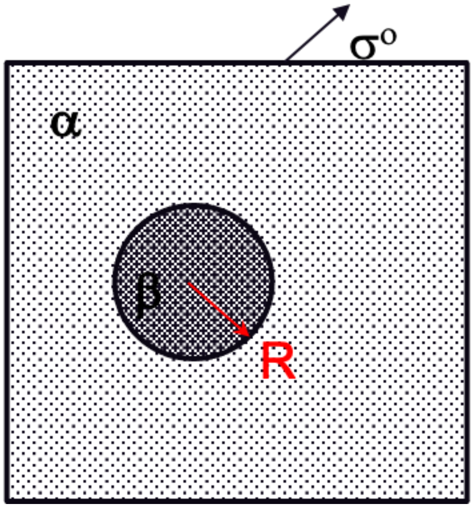

Figure 3.1: Configurations of the precipitate nucleus with radius R inside the matrix

The objective is to map out the Gibbs free energy landscape of the configurations with respect to the applied stress (both the hydrostatic and deviatoric components), temperature, nucleus size, and nominal concentration. This allows calculating the difference in free energy between a configuration with a nucleus of a specific size under applied stress and that of non precipitated matrix. This change in the Gibbs free energy between the two systems determines whether it is energetically favorable for the nucleus to form and grow. From this, the steady state and transient nucleation rates can be determine as shown in previous section.

3.3.1 Eshelby inhomogeneous inclusion treatment of the precipitate nucleus

To determine the mechanical fields within the precipitate nucleus, the standard approach proposed by Eshelby is adopted where the β nucleus is treated as an inhomogeneous inclusion with elastic constants (C^*_{ijkl}) embedded in a matrix with constants (C_{ijkl}) as seen in Fig.3.1. In addition, there is a transformation eigenstrain ε^{tr}_{kl}, which is the required strain for the formation of the precipitate. This strain is expected to vary depending on the state of coherency of the second phase. In what follows, the general Eshelby treatment for the inhomogeneous inclusion problem will be discussed. More details can be found in [35]. While the model relies on simplifying assumptions such as linear elasticity and small strains, it can be used to qualitatively demonstrate the role of stress on the precipitate nucleation. Importantly, this approach captures both the effect of the inhomogeneity (differences in elastic stiffness between the matrix and the precipitate) and the misfit strain (by accounting for the strain required for transformation). Einstein summation convention over repeated indices is utilized for all expressions in the following discussion. For a system under a uniform strain ε^o due to the uniformly applied stress σ^o, the stress inside the inhomogeneous inclusion can be equivalently written as:

$$\sigma_{ij}^o + \Delta\sigma_{ij} = C_{ijkl}^* \left(\varepsilon_{kl}^o + \Delta\varepsilon_{kl} - \varepsilon_{kl}^{tr}\right) \tag{3.12}$$

where $\Delta\sigma$ and $\Delta\varepsilon$ are the deviations to the stress and strain caused by the inhomogeneous inclusion. The transformation strain (ε^{tr}) is the strain accommodating for the lattice misfit between the matrix and the precipitates. One approach to solve the inhomogeneous inclusion problem is to use the equivalent homogeneous inclusion with an additional fictitious transformation strain (ε^*) which is determined via the use of the Eshelby solution. The stress inside the inhomogeneous inclusion then can be rewritten as:

$$\sigma_{ij}^o + \Delta\sigma_{ij} = C_{ijkl} \left(\varepsilon_{kl}^o + \Delta\varepsilon_{kl} - \varepsilon_{kl}^{tr} - \varepsilon_{kl}^*\right) \tag{3.13}$$

Importantly, the deviation of the strain due to the inhomogeneous inclusion is related to the sum of the transformation and fictitious strains $\varepsilon_{mn}^{**} = (\varepsilon_{mn}^{tr} + \varepsilon_{mn}^*)$ such as:

$$\Delta\varepsilon_{kl} = S_{klmn}\varepsilon_{mn}^{**} \tag{3.14}$$

where S_{klmn} is the Eshelby tensor. Here, the inhomogeneous inclusion is assumed to be a sphere and the standard Eshelby solution dictates that the stress field is homogeneous for an ellipsoidal-shaped inclusion [35]. Substituting the difference in elastic stiffness tensor as $\Delta C_{ijkl} = C_{ijkl}^* - C_{ijkl}$, one can derive the following equation:

$$\left(\Delta C_{ijkl}S_{klmn} + C_{ijmn}\right)\varepsilon_{mn}^{**} = -\Delta C_{ijkl}C_{klmn}^{-1}\sigma_{mn}^o + C_{ijkl}^*\varepsilon_{kl}^{tr} \tag{3.15}$$

where S_{klmn} is the Eshelby tensor, which has an analytical solution for spherical precipitates. Importantly, this expression allows one to determine the fictitious strain (ε^*) and thus calculate, the deviations to the stress and strain ($\Delta\sigma$ and $\Delta\varepsilon$) caused by the inhomogeneous inclusion given the applied stress tensor. With those deviations in stress and strain, one can obtain the elastic fields inside the precipitates as a function of the applied stress tensor that can contain both the hydrostatic and deviatoric components.

3.3.2 Determination of nucleus' composition via parallel tangent construction

In this section, the standard chemical potential is expanded into the chemo-mechanical potential to capture both the effects of chemical compositions and stress on the Gibbs free energy. An improved algorithm for the parallel tangent construction to determine the activation barrier is discussed where the mole fraction and corresponding chemo-mechanical potential of the matrix can be calculated (instead of assuming to be a constant related to the nominal concentration). The Gibbs free energy of the homogeneous system of phase α under a constant applied stress state σ^o and temperature T can be approximated by:

$$G^\alpha\left(\sigma_o, T\right) = \sum_{i=A,B} \nu_i^\alpha\left(\sigma_o, T\right)N_i^\alpha \tag{3.16}$$

where

$$\nu_i^\alpha\left(\sigma_o, T\right) = \mu_i^\alpha\left(T\right) + \frac{V^\alpha(T, N_i^\alpha)}{2}\sigma_o : S^\alpha\left(T, x_i^\alpha\right) : \sigma_o \tag{3.17}$$

Here, $\nu_i^\alpha\left(\sigma_o, T\right)$ is the chemo-mechanical potential that includes both the chemical potential $\left(\mu_i^\alpha\left(\sigma_o, T\right)\right)$ and the elastic strain energy density. N_i^α is the number of mols of component i^{th} in phase α, V^α is the volume of phase α which equals to the total volume of the system in this case, S^α is the elastic compliance tensor of phase α, which depends on both the temperature of the system and the mole fractions. For simplicity, S^α and V^α are assumed to be linearly dependent on the mole fractions/concentrations. Normalizing the above equation by the number of mols (N) gives the molar Gibbs free energy:

$$\frac{G^\alpha\left(\sigma_o, T\right)}{N} = \sum_{i=A,B}\mu_i^\alpha\left(T\right)x_i^\alpha + \frac{V_M^\alpha(T, x_i^\alpha)}{2}\sigma_o : S^\alpha\left(T, x_i^\alpha\right) : \sigma_o \tag{3.18}$$

where V_M^α is the molar volume of phase α, which also depends on the temperature and the mole fraction of each component within phase α. The chemical potential is calculated by:

$$\mu_A^\alpha\left(T\right) = \mu_{A,o}^\alpha\left(T\right) + \left(1 - x_A^\alpha\right)^2\left(\omega_A^\alpha + 2x_A\left(\omega_B^\alpha - \omega_A^\alpha\right)\right) + RTln\left(x_A^\alpha\right) \tag{3.19}$$

where ω is called the interchange energy (or the Margules interaction parameter). Specifically, it accounts for the correction in interaction energies between each atom with surrounding atoms in the solid solutions. Here, the asymmetric solution model is used with four independent interchange energies ω_A^α, ω_B^α, ω_A^β, and ω_B^β. This allows us to capture the complex G-x curve behavior of Fe-Cr system as shown later in the result. The difference in chemical potential is often referred to as the diffusion potential, M_{BA}^α, defined as [36]:

$$M_{BA}^\alpha = \mu_B^\alpha - \mu_A^\alpha = \frac{\partial}{dx_A^\alpha}\left(\frac{G^\alpha\left(\sigma_o, T\right)}{N}\right) \tag{3.20}$$

This difference in chemical potential arises because the process of changing the mole fraction requires the addition or removal of a B atom and simultaneously the removal or addition of an A atom, respectively, and the corresponding energy change results in the differences in the chemical potentials. For a critical nucleus in (unstable) equilibrium with the surrounding matrix, the diffusion potentials between the two must be the same:

$$M_{BA}^\alpha = M_{BA}^\beta \tag{3.21}$$

This condition states that species can change phase at not cost to the systems energy. Note however that each of the specie has not reached a true thermodynamic equilibrium. Substituting Eqs. 3.18, 3.19, and 3.20 in, we have:

$$\begin{aligned}
&\mu_{A,o}^\alpha\left(T\right) - \mu_{B,o}^\alpha\left(T\right) + RTln\left(\frac{\acute{x}_A^\alpha}{1 - \acute{x}_A^\alpha}\right) + \left(1 - \acute{x}_A^\alpha\right)^2\left(\omega_A^\alpha + 2\acute{x}_A^\alpha\left(\omega_B^\alpha - \omega_A^\alpha\right)\right) \\
&- \left(\acute{x}_A^\alpha\right)^2\left(\omega_B^\alpha + 2\left(1 - \acute{x}_A^\alpha\right)\left(\omega_A^\alpha - \omega_B^\alpha\right)\right) + \frac{\partial}{d\acute{x}_A^\alpha}\left(\frac{V_M(T, \acute{x}_A^\alpha)}{2}\sigma_o : S^\alpha\left(T, \acute{x}_A^\alpha\right) : \sigma_o\right) = \\
&\mu_{A,o}^\beta\left(T\right) - \mu_{B,o}^\beta\left(T\right) + RTln\left(\frac{\acute{x}_A^\beta}{1 - \acute{x}_A^\beta}\right) + \left(1 - \acute{x}_A^\beta\right)^2\left(\omega_A^\beta + 2\acute{x}_A^\beta\left(\omega_B^\beta - \omega_A^\beta\right)\right) \\
&- \left(\acute{x}_A^\beta\right)^2\left(\omega_B^\beta + 2\left(1 - \acute{x}_A^\beta\right)\left(\omega_A^\beta - \omega_B^\beta\right)\right) + \frac{\partial}{d\acute{x}_A^\beta}\left(\frac{V_M(T, \acute{x}_A^\beta)}{2}\sigma_i : S^\beta\left(T, \acute{x}_A^\beta\right) : \sigma_i\right)
\end{aligned} \tag{3.22}$$

where $\acute{x}_A^\alpha$ is the mole fraction of component A in phase α after the nucleus is formed. σ^i is the stress state inside the precipitate, which was derived in the previous section. We can further simplify the above equation into:

$$\acute{x}_A^\beta = \frac{\acute{x}_A^\alpha}{K\left(1-\acute{x}_A^\alpha\right)+\acute{x}_A^\alpha} \tag{3.23}$$

where

$$K = e^{\frac{\mu_{A,o}^\beta(T)-\mu_{B,o}^\beta(T)-\mu_{A,o}^\alpha(T)+\mu_{B,o}^\alpha(T)-\left(1-\acute{x}_A^\alpha\right)^2\left(\omega_A^\alpha+2\acute{x}_A^\alpha\left(\omega_B^\alpha-\omega_A^\alpha\right)\right)+\left(\acute{x}_A^\alpha\right)^2\left(\omega_B^\alpha+2\left(1-\acute{x}_A^\alpha\right)\left(\omega_A^\alpha-\omega_B^\alpha\right)\right)}{RT}}$$
$$e^{\frac{\left(1-\acute{x}_A^\beta\right)^2\left(\omega_A^\beta+2\acute{x}_A^\beta\left(\omega_B^\beta-\omega_A^\beta\right)\right)-\left(\acute{x}_A^\beta\right)^2\left(\omega_B^\beta+2\left(1-\acute{x}_A^\beta\right)\left(\omega_A^\beta-\omega_B^\beta\right)\right)\frac{\partial}{d\acute{x}_A^\beta}\left(\frac{V_M\left(T,\acute{x}_A^\beta\right)}{2}\sigma_i:S\left(T,\acute{x}_A^\beta\right):\sigma_i\right)-\frac{\partial}{d\acute{x}_A^\alpha}\left(\frac{V_M\left(T,\acute{x}_A^\alpha\right)}{2}\sigma_o:S\left(T,\acute{x}_A^\alpha\right):\sigma_o\right)}{RT}} \tag{3.24}$$

Even though the expression looks quite lengthy, K is a function of the mole fractions of both the matrix and precipitate.
Further, we imposed mass conservation. This is expressed as follows:

$$N_A = \acute{x}_A^\alpha\left(N-\Delta\mathrm{N}\right)+\acute{x}_A^\beta\left(\Delta\mathrm{N}\right) \tag{3.25}$$

Combining these two above equations, we end up with the nonlinear systems of equations that we need to solve:

$$\begin{cases} \acute{x}_A^\alpha\left(N-\Delta\mathrm{N}\right)+\frac{\acute{x}_A^\alpha}{K\left(1-\acute{x}_A^\alpha\right)+\acute{x}_A^\alpha}\left(\Delta\mathrm{N}\right)-N_A=0 \\ \acute{x}_A^\beta-\frac{\acute{x}_A^\alpha}{K\left(1-\acute{x}_A^\alpha\right)+\acute{x}_A^\alpha}=0 \end{cases} \tag{3.26}$$

where N_A is the number of A atoms in the matrix. For each precipitate radius, one can solve for the mole fractions ($\acute{x}_A^\alpha$ and $\acute{x}_A^\beta$) or compositions of the matrix and the precipitate using Eq. 3.26. Since K is a function of those mole fractions, this system of equation is nonlinear and has to be solved numerically using the Broyden method. Note that conventional approaches only post process concentration evolution.

3.3.3 Energetic consideration of a binary system under an applied stress

The derived mechanical and chemical quantities are then used to calculate the difference in Gibbs free energy between the system with and without the precipitate, which gives an estimate of the energy barrier for the formation of the precipitate. The change in Gibbs free energy due to the precipitate is given by

$$\Delta\mathrm{G} = G_1-G_o = E_1+E_{ch,1}+\Gamma-E_o-E_{ch,0} \tag{3.27}$$

where E_o and E_1 are the elastic strain energy of the systems without and with the precipitate, while Γ is the total interfacial energy of the interfaces shared between the precipitate and the matrix. $E_{ch,0}$ and $E_{ch,1}$ are the Gibbs chemical free energy of the systems without and with the precipitate. The Gibbs mechanical free energy of a medium undergoing a transformation strain (ε^{tr}_{kl}) under an externally applied stress (σ^{o}_{ij}) to form a precipitate is given by

$$E_1 = \frac{1}{2}\int_D \left(\sigma^o_{ij} + \Delta\sigma_{ij}\right)\left(\varepsilon^o_{kl} + \Delta\varepsilon_{kl} - \varepsilon^{tr}_{kl}\right) dD - \int_S F_i\left(u^o_i + \Delta u_i\right) dS \tag{3.28}$$

where F_i are the components of the external surface traction, u^o_i is the displacement if F_i acts alone, and Δu_i is the displacement induced by the precipitate. D and S are the volume and external surface of the medium, respectively. From the derivation by Mura [35], this elastic strain energy of the system with the precipitate becomes

$$E_1 = \frac{1}{2}\int_D \sigma^o_{ij}\varepsilon^o_{ij} dD - \frac{1}{2}\int_\Omega \Delta\sigma_{ij}\varepsilon^{tr}_{ij} dD + \frac{1}{2}\int_\Omega \sigma^o_{ij}\varepsilon^*_{ij} dD - \int_S F_i\left(u^o_i + \Delta u_i\right) dS \tag{3.29}$$

where Ω is the volume of the precipitate. Moreover, the Gibbs mechanical free energy for the homogenous matrix is given by

$$E_o = \frac{1}{2}\int_D \sigma^o_{ij}\varepsilon^o_{kl} dD - \int_S F_i u^o_i dS \tag{3.30}$$

Based on the previous section, the Gibbs chemical free energy of the homogenous medium is:

$$E_{ch,0} = \sum_{i=A,B} \mu^\alpha_i\left(\sigma_o, T\right) x^\alpha_i \tag{3.31}$$

Similarly, the Gibbs chemical free energy for the system with the nucleus with radius of R (and number of mols ΔN) is:

$$E_{ch,1} = \frac{N - \Delta\mathrm{N}}{N}\left(\sum_{i=A,B} \acute{\mu}^\alpha_i\left(\sigma_o, T\right)\acute{x}^\alpha_i\right) + \frac{\Delta\mathrm{N}}{N}\left(\sum_{i=A,B} \acute{\mu}^\beta_i\left(\sigma_o, T\right)\acute{x}^\beta_i\right) \tag{3.32}$$

Here, $\acute{x}^\alpha_i$ and $\acute{x}^\beta_i$ are the mole fractions of the system. From Eqs 5-9, one can calculate the change in normalized Gibbs free energy due to the inhomogeneous inclusion as:

$$\begin{aligned}\frac{\Delta\mathrm{G}}{N} = {} & \frac{N - \Delta\mathrm{N}}{N}\left(\sum_{i=A,B} \acute{\mu}^\alpha_i \acute{x}^\alpha_i\right) + \frac{\Delta\mathrm{N}}{N}\left(\sum_{i=A,B} \acute{\mu}^\beta_i \acute{x}^\beta_i\right) - \left(\sum_{i=A,B} \mu^\alpha_i x^\alpha_i\right) + \\ & \frac{4\pi R^3}{3N}\left(-\frac{1}{2}\Delta\sigma_{ij}\varepsilon^{tr}_{ij} - \frac{1}{2}\Delta\sigma^o_{ij}\varepsilon^*_{ij} + \sigma^o_{ij}\varepsilon^{tr}_{ij}\right) + 4\pi R^2\gamma\end{aligned} \tag{3.33}$$

Here, γ is the average surface energy. Importantly, this expression allows calculating the minimum energy barrier required to stabilize an inhomogeneous inclusion as a function of size and externally applied stresses.

3.4 Nucleation model results

The results reported in this section are determined using the model described in the previous section for the Fe-Cr systems with the γ-Fe matrix and the σ precipitate. A majority of the discussion will focus on the effects of chemical potential and the combined chemo-mechanical potential on the nucleation energy barrier, and corresponding nucleation rate. Two different solid solution models are used to demonstrate the capability of our approach: ideal (with no interchange energies, $\omega = 0$) and regular solutions. The latter being more representative of austenitic steels.

3.4.1 With ideal solution

3.4.1.1 Case 1: Chemical effects

As a first application of the model, pyCalphad was used to generated a G-X curve for a model Fe-Cr system. Further, the quantification of the activation energy, critical and stable radii will be made by considering only contribution from the chemical driving forces. Figure 3.2 shows the free energy - mole fraction (G-X) curves for the Fe-Cr systems that will be investigated in this work. We extract a simplified G-X curve from this dataset by considering an ideal solution first (i.e. no spinoidal driving forces). Naturally, compared to the G-X curve from PyCalphad, our ideal solid solution model only matches qualitatively where the difference in Gibbs free energy between the precipitate (σ) and the matrix ($\gamma - Fe$) changes from negative to positive as the Cr concentration is increased. The parameters for the model can be found in Table 3.1. Here, the system contain 1 billion atoms, and the nominal concentration of Cr is 20%. α phase denotes the matrix ($\gamma - Fe$) and β phase represents the σ precipitate.

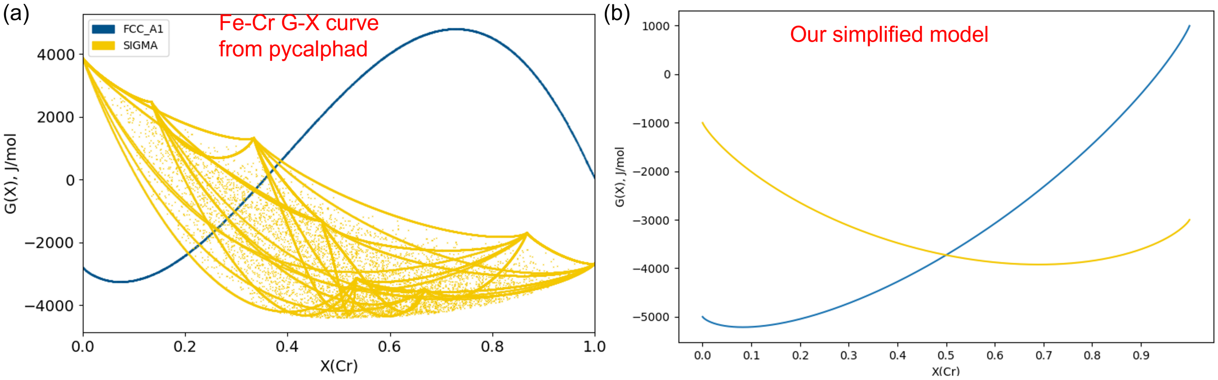

Figure 3.2: Free energy - mole fraction curves for (Fe-Cr) systems from (a) pycalphad and (a) ideal solution model

Table 3.1: Ideal solid solution model parameter

Parameter	Value	Unit
μ^{α}_{Fe}	-5	kJ/mol
μ^{α}_{Cr}	1	kJ/mol
μ^{β}_{Fe}	-1	kJ/mol
μ^{β}_{Cr}	-3	kJ/mol

Figure 3.3 demonstrates the dynamic nature of our approach where the change in Gibbs free energy can be determined and tracked as a function of the nucleus size.

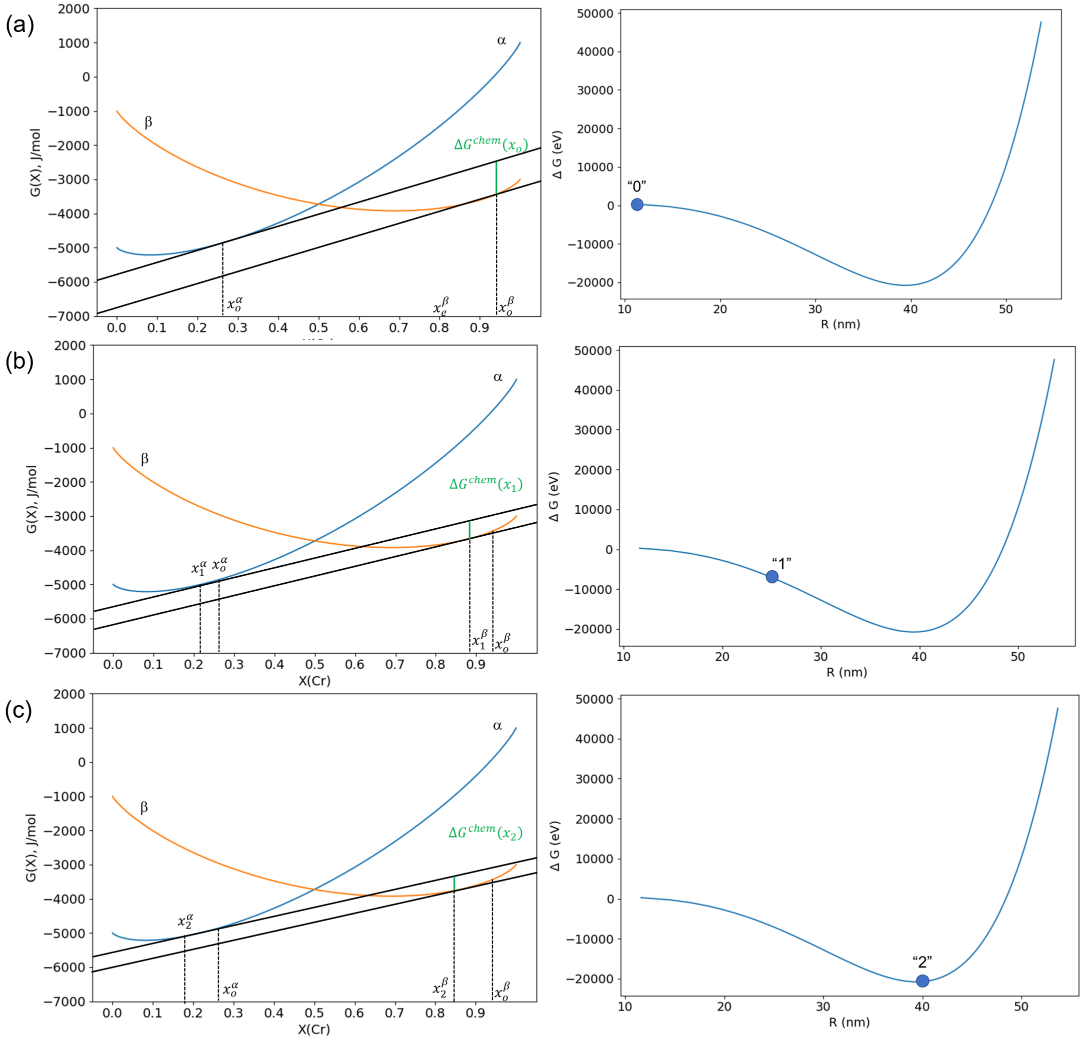

Figure 3.3: Ideal solution models for (Fe-Cr) systems with updating concentrations as a function of the precipitate nuclei of (a) 12 nm, (b) 26 nm, and (c) 40 nm

Instead of fixing the composition matrix to be the nominal concentration (in the conventional tangent construction method), our method allows updating the composition and corresponding diffusional potential (slope of the G- curve) depending on the size of the precipitate nucleus. As a result, not only the critical radius (corresponding to the local maximum of the G-x curve) but also the stable radius of the precipitate can be determined. Importantly, the results from our method are insensitive to the choice of matrix/precipitate volumes, which is not the case for conventional tangent construction method.

Figure 3.4 (a) shows the difference in Gibbs free energy between the systems with and without the precipitate and the enlarged portion of the local maximum of the curve representing the critical radius and corresponding activation energy barrier. With only considering the chemical driving force, the critical radius is approximately 9 nm with the energy activation barrier of about 403 eV, which is extremely high. Fig 3.4 (b) shows the reduction in mole fraction of Cr in α and β phases for larger precipitate, which can only be obtained using our updated method.

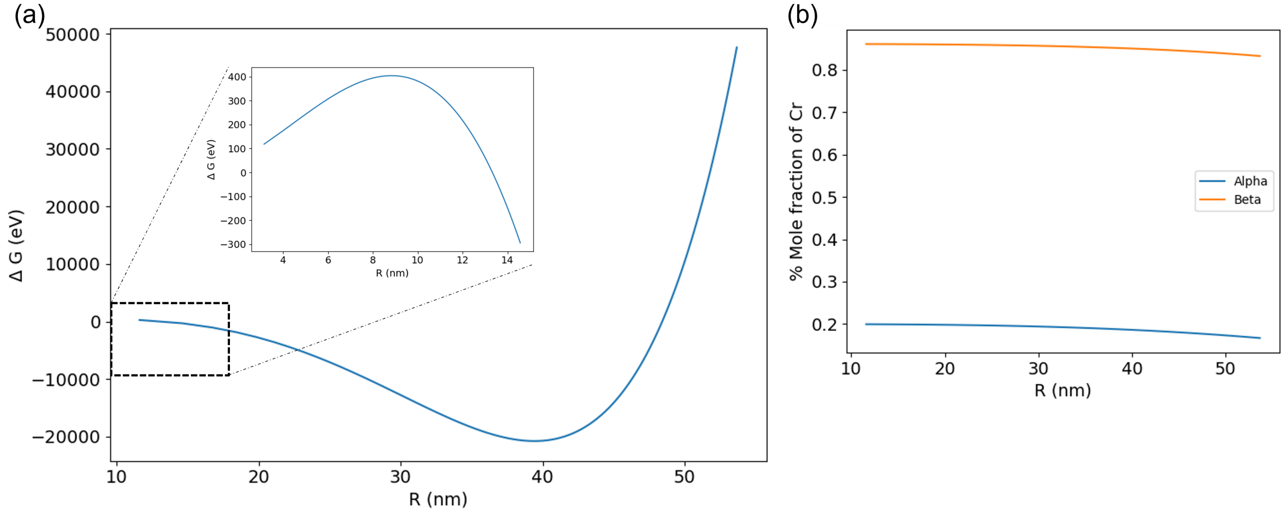

Figure 3.4: (a) Difference in Gibbs free energy between the systems with and without the precipitate for the ideal solution model (b) the mole fraction of Cr in α and β phases as a function of the precipitate radius

3.4.1.2 Case 2: Considerations of both chemical and mechanical effects

In this second application, we now consider the effects of mechanical loads (remotely applied) on the thermodynamics driving forces and unstabel and stable configurations. Table 3.2 contains the elastic constants used in this work. This is adopted from the values reported in the potential paper for pure FCC Fe and Cr [37]. For each composition, the elastic constants are linearly interpolated using the mole fraction and elastic constants of each element. The elastic constants of the precipitates are either half (softer) or double (stiffer) the corresponding constants of the matrix for the same composition. The transformation strain is assumed to be $\begin{bmatrix} -0.05 & 0 & 0 \\ 0 & 0.05 & 0 \\ 0 & 0 & 0 \end{bmatrix}$. This is qualitatively consistent with expected values for some precipitates. In this example, the applied stress is $\begin{bmatrix} 1 & 0 & 0 \\ 0 & -1 & 0 \\ 0 & 0 & 0 \end{bmatrix}$ GPa. Such large value is used to illustrate the potential effects of mechanical loads. We note that in AM systems, one expects internal stresses to reach several hundres of MPa. As such, the example presented should illustrate likely effects of internal mechanical fields.

Figure 3.5 compares the activation energy barrier for precipitate nucleation and corresponding critical radius for different scenarios with and without the mechanical contributions. It is found that the elastic strain energy from the difference in stiffness (also known as inhomogeneity effects) has a weaker effects on the results compared to the the transformation strain energy. Given the extreme assumption of high applied stress and large difference in

Table 3.2: Elastic constants of FCC Fe and Cr(in GPa)

Parameter	Fe	Cr
C_{11}	84.567	185.2
C_{22}	84.567	185.2
C_{33}	84.567	185.2
C_{12}	49.309	137.661
C_{13}	49.309	137.661
C_{23}	49.309	137.661
C_{44}	20.875	133.908

stiffness between the matrix and precipitate, the contribution of the elastic strain energy is quite insignificant. This likely justifies the assumption of ignoring the pressure-dependence term in the Gibbs free energy calculation for most material systems. [32]. On the other hand, the effects of including the transformation is quite significant with an order of magnitude reduction in activation energy barrier. Even though the activation barrier remains relatively high (29 eV), it demonstrates the effects of transformation strain (to accommodate for the mismatch in lattice between the precipitate and the matrix) on the overall activation barrier, which has been greatly ignored.

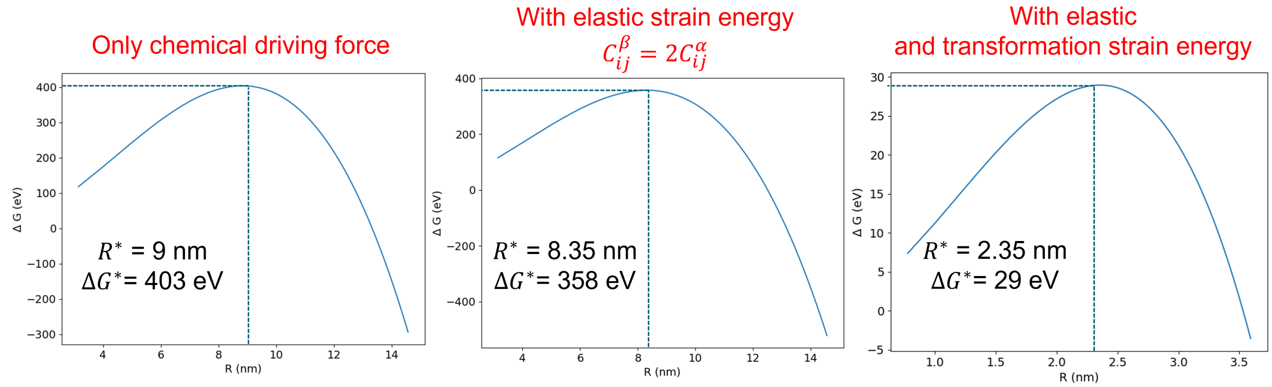

Figure 3.5: Activation energy barrier and critical radius for (a) only chemical driving force, (b) with chemical and elastic strain energy and (c) with chemical, elastic and transformation strain energy

3.4.2 With regular solid solution

While the results from the ideal solution is quite promising, it only qualitatively represents our problems. Thus, a regular solid solution model is used and coupled with the developed nucleation model to better quantify the effects of the transformation strain on the nucleation of the σ precipitate in 316 austenitic stainless steel (SS). Figure 3.6 shows the free energy - mole fraction (G-X) curves for the Fe-Cr systems that will be investigated in this work. With the regular solution model, we can perfectly fit our model to the G-X curve from PyCalphad. The parameters for the model can be found in Table 3.3.

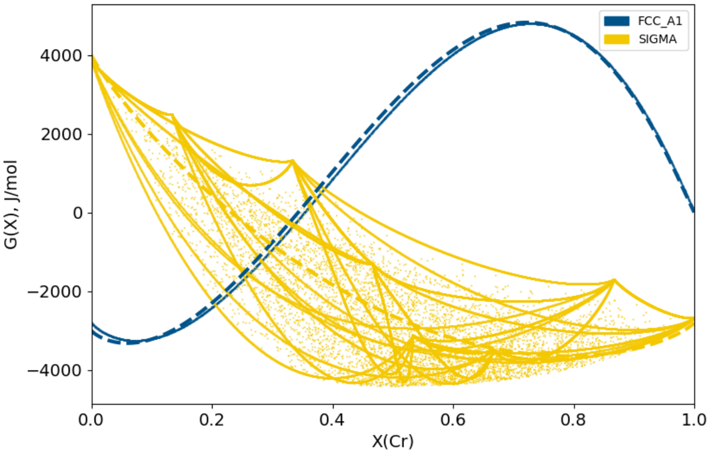

Figure 3.6: Free energy - mole fraction curves for (Fe-Cr) systems from (a) pycalphad and regular solution model (dashed line)

Table 3.3: Regular solid solution model parameter

Parameter	Value	Unit
μ_{Fe}^{α}	-5	kJ/mol
μ_{Cr}^{α}	1	kJ/mol
μ_{Fe}^{β}	-1	kJ/mol
μ_{Cr}^{β}	-3	kJ/mol
ω_{Fe}^{α}	-2	kJ/mol
ω_{Cr}^{α}	50	kJ/mol
ω_{Fe}^{β}	-6	kJ/mol
ω_{Cr}^{β}	-6	kJ/mol

3.4.2.1 *Effects of transformation strain and applied stress on the critical radius and activation energies*

The objective here is to map the likely effects of mechanical loads and internal stress fields on precipitation. For the sake of comprehensiveness and given that each precipitate type that forms can induce different mechanical fields, distinct cases will be studied. Further, the initial composition of the system as well as the remotely applied loads will be varied. Here, the system contain 1 billion atoms, and two nominal concentrations of 5 and 12 % of Cr are used. The stiffness tensor of the precipitate is exactly the same as the matrix. Two transformation strain tensors are used, which are $\begin{bmatrix} -0.05 & 0 & 0 \\ 0 & -0.05 & 0 \\ 0 & 0 & 0 \end{bmatrix}$ and $\begin{bmatrix} -0.05 & 0 & 0 \\ 0 & 0.05 & 0 \\ 0 & 0 & 0 \end{bmatrix}$. To evaluate the role of stress state, a wide range of stress states are investigated $\begin{bmatrix} \sigma_{xx}^{o} & 0 & 0 \\ 0 & \sigma_{yy}^{o} & 0 \\ 0 & 0 & 0 \end{bmatrix}$ where σ_{xx}^{o} and σ_{yy}^{o} ranges from -1.0 to 1.0 GPa with increment of 0.2 GPa, which result in 100 combinations of stress states.

The goal is to determine the activation energy for each of these 100 cases for both transformation strains at two different nominal mole fractions to evaluate the effects of stress on the nucleation.

Figure 3.7 compares the activation energy barrier for precipitate nucleation for different scenarios of applied stress, transformation strain, and initial mole fraction. With only chemical considerations, the activation energy barriers for the case with initial mole fractions of 5% and 12 % are 6.1 and 296 eV, respectively. As shown in Fig. 3.7, adding the effects of stress and transformation strain can reduce these activation energy barriers which lead to higher nucleation rates. Even at zero applied stress, the activation energy barriers are lower. The cases with the initial mole fraction of 5% has more significant reduction in energy barrier compared to the ones with initial mole fraction of 12%. Specifically, for the case with initial mole fraction of 5%, the activation energy barrier can be reduced down to 10 eV, which is almost 30 times smaller than in the case where only the chemical driving force is considered. This is because the chemical driving force is much lower for the cases with initial mole fraction of 12 % (shows in the large energy barrier). In those cases, the mechanical contributions become dominant and can significantly reduce the energy barrier.

Qualitatively, for each transformation strain, the effects of stress states seems similar. For instance, for a more deviatoric transformation strain of $\begin{bmatrix} -0.05 & 0 & 0 \\ 0 & 0.05 & 0 \\ 0 & 0 & 0 \end{bmatrix}$, the applied stress with the negative σ^o_{xx} and positive σ^o_{yy} results in the maximum reduction in activation barrier, while loading in the opposite direction would increase the activation barrier. On the other hand, for a more hydrostatic transformation strain of $\begin{bmatrix} -0.05 & 0 & 0 \\ 0 & -0.05 & 0 \\ 0 & 0 & 0 \end{bmatrix}$, the maximum reduction in activation barrier is observed for $\sigma^o_{xx} = \sigma^o_{yy} = 1$ GPa. Thus, both the transformation strain and the applied stress states have a great role in the determination of the activation energy barriers for nucleation and thus the nucleation rates of the precipitates.

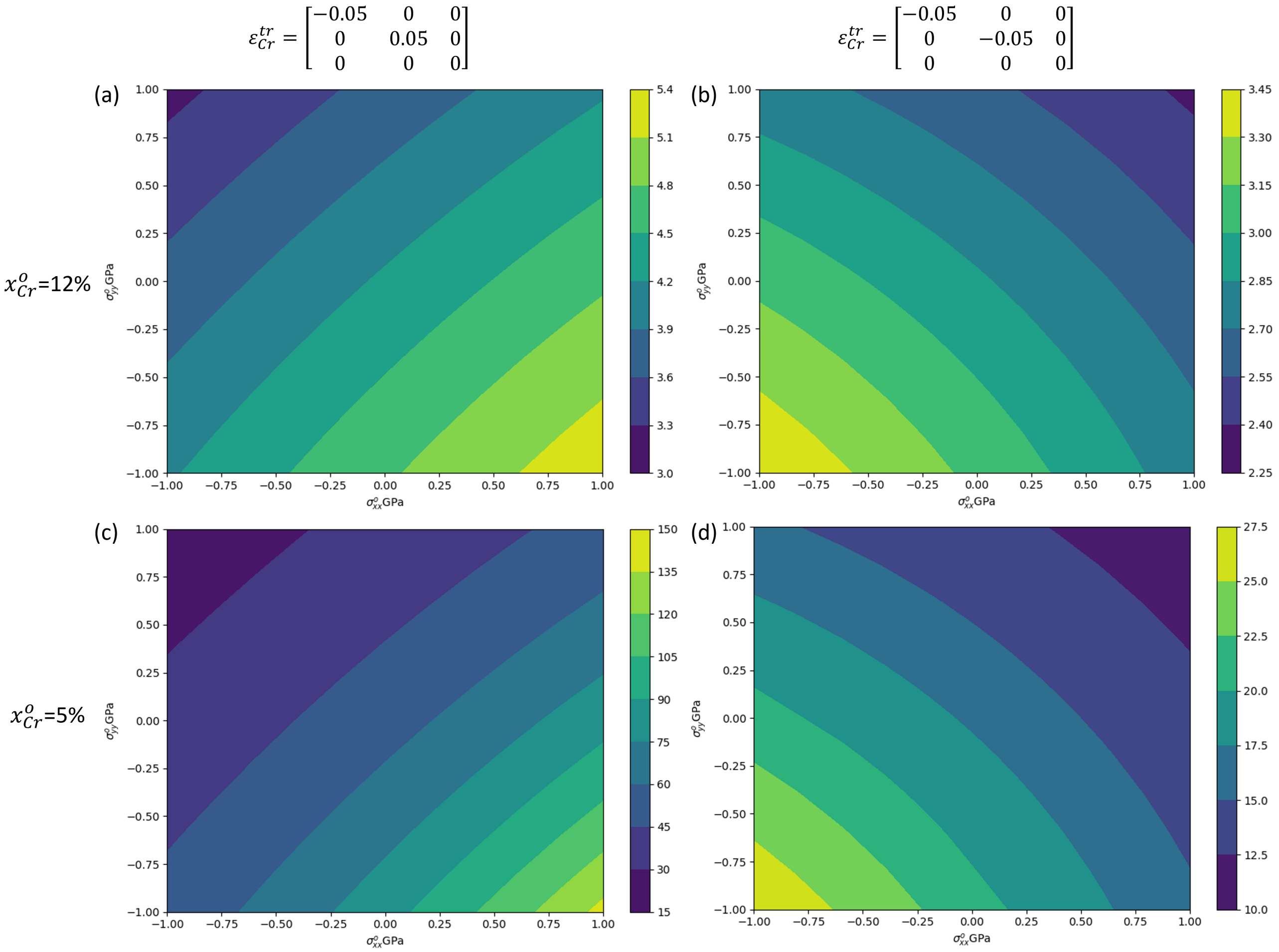

Figure 3.7: Activation energy barrier (eV) for different applied stress states (σ_{xx}^{o} and σ_{yy}^{o}) for initial mole fraction of 5% (a) and (b) and 12% (c) and (d). Two different transformation strains are used: $\begin{bmatrix} -0.05 & 0 & 0 \\ 0 & 0.05 & 0 \\ 0 & 0 & 0 \end{bmatrix}$ for (a) and (c) and $\begin{bmatrix} -0.05 & 0 & 0 \\ 0 & -0.05 & 0 \\ 0 & 0 & 0 \end{bmatrix}$ for (b) and (d)

4 Preliminary models for the effect of dislocation and grain structure on creep and aging

4.1 The effect of grain structure on creep anisotropy

Creep tests on additively manufactured (AM) materials, including laser powder bed fusion stainless steel, have been shown to exhibit strong anisotropy. While the literature on the creep behavior of laser powder bed fused (LPBF) 316H stainless steel remains limited, some works on similar materials have tried to shed some light on this anisotropic behavior with respect to the build and loading directions.

Although the precise mechanism and the source of the anisotropy is not clear, some recent works on LPBF IN718 have studied this phenomena and found varying explanations. Ghorbanpour et al. [38], for instance, studied the deformation at high temperature and looked at various loading directions with respect to build direction and attributed the plastic anisotropy to grain structure and texture. Shi et al.'s [39] tests had a shorter creep life when loaded perpendicular to the build direction. They attributed this anisotropy to grain boundaries being primarily distributed perpendicular to the loading direction, which could be likely regions for creep void formation. Examining a closely related material, 316L stainless steel, Williams et al. [40] identified higher grain boundary diffusion as a contributing factor to anisotropy when grain boundaries were oriented normal to the maximum principal stress. They report eight times higher creep rates when the sample is loaded perpendicular to the build direction.

Among the numerous factors that can cause anisotropic creep response, this subsection examines the influence of grain structure. In the absence of actual LPBF 316H creep test data, we used previously-calibrated wrought 316H material parameters in a MOOSE-based CPFEM framework, DEER to simulate creep in LPBF 316H. However, we simulated realistic LPBF grain structures. This study therefore considers the effect of grain structure independent from any changes to the grain-scale material constitutive behavior, for example the effect of dislocation structure or different precipitation hardening mechanisms. LPBF microstructures often exhibit long columnar grains along the build direction so we start by examining the impact of these columnar grains on the predicted creep behavior of the material. All the microstructures considered in the subsequent subsections have been subjected to 130 MPa of tensile stress along the respective directions at a temperature of 600° C. The details of CPFEM model used here can be found in [41].

4.1.1 Creep in prismatic polycrystals

In a simplified scenario, we begin by examining a prismatic microstructure with 16 randomly oriented grains (Fig. 4.1). When loaded along different directions, we see the expected anisotropy where the longer direction (z) shows higher creep strain due to the longer slip path available in each singularly oriented grain. So, in absence of barrier to slip via dislocation glide, we see higher strain along z as the material creeps. A larger polycrystal would produce similar creep curves in the other two directions, however the sample effect here causes the x and y curves to be substantially different in this simulation. All three directions show faster creep as compared to the aggregate behavior in a polycrystalline material, as modeled through a Taylor model simulation using the same orientations.

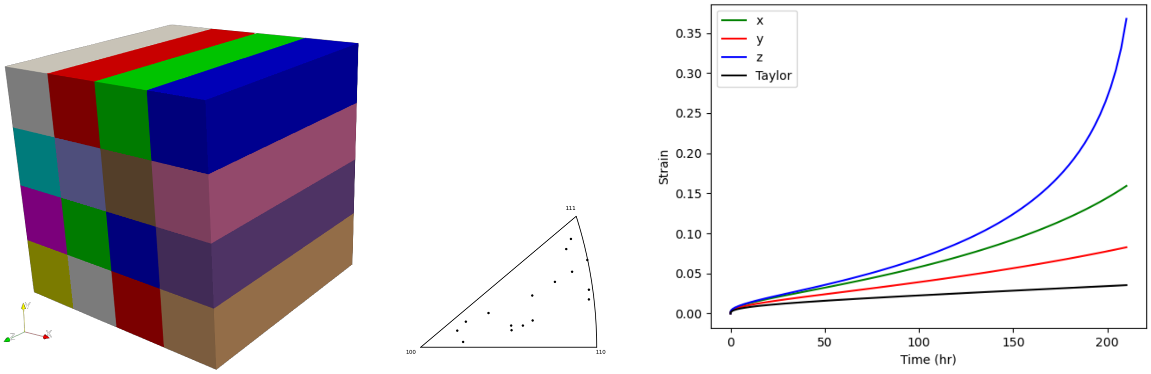

Figure 4.1: A 16 grained prismatic microstructure, an inverse pole figure showing no preferred orientations and the creep response.

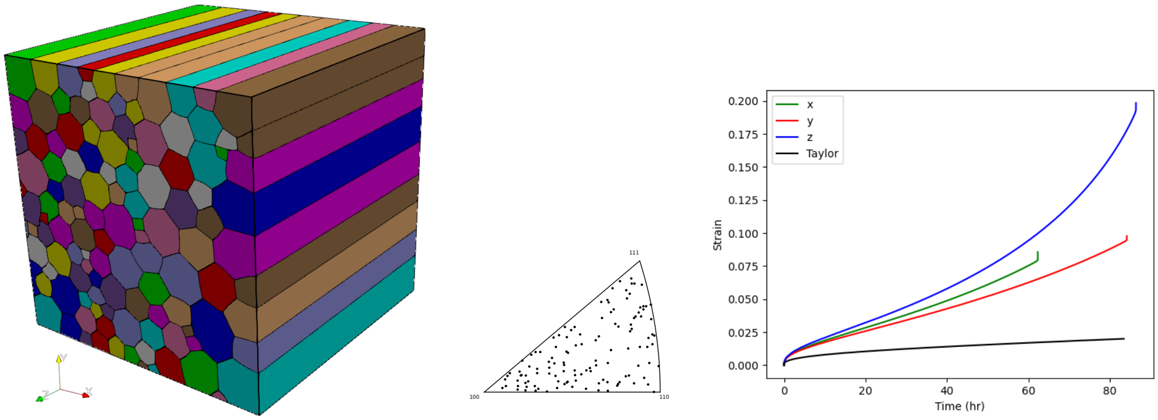

Figure 4.2: A 125 grained columnar microstructure, an inverse polefigure showing no preferred orientations and the creep response.

Adding more complexity to the polycrystal model, a larger polycrystal is generated using Neper [42] where a tessellation of 125 grains is generated and used to create a columnar grain structure. In this case, we have a more randomized grain structure in $x - y$ plane but still a prismatic structure along z. Fig. 4.2 shows the polycyrstal, an inverse pole figure that shows no preferential texture in the random orientations chosen for the grains, and the creep response as a result of loading along different directions and comparing them to the aggregate behavior in the Taylor model. Similar to the previous case, we see higher strain along z owing to the unimpeded slip path. The curves for the x and y directions are now more similar, as this simulation samples a larger number of grains.

Having established the anisotropic creep response is at least partially a result of the grain structure in the prismatic microstructures, we will now examine the impact of the aspect ratio of the the columnar grains. This will help us understand how the grain diameter to length ratio may influence creep response in the prismatic grains and help us better understand which morphological factors contribute the creep behavior observed in the AM microstructures.

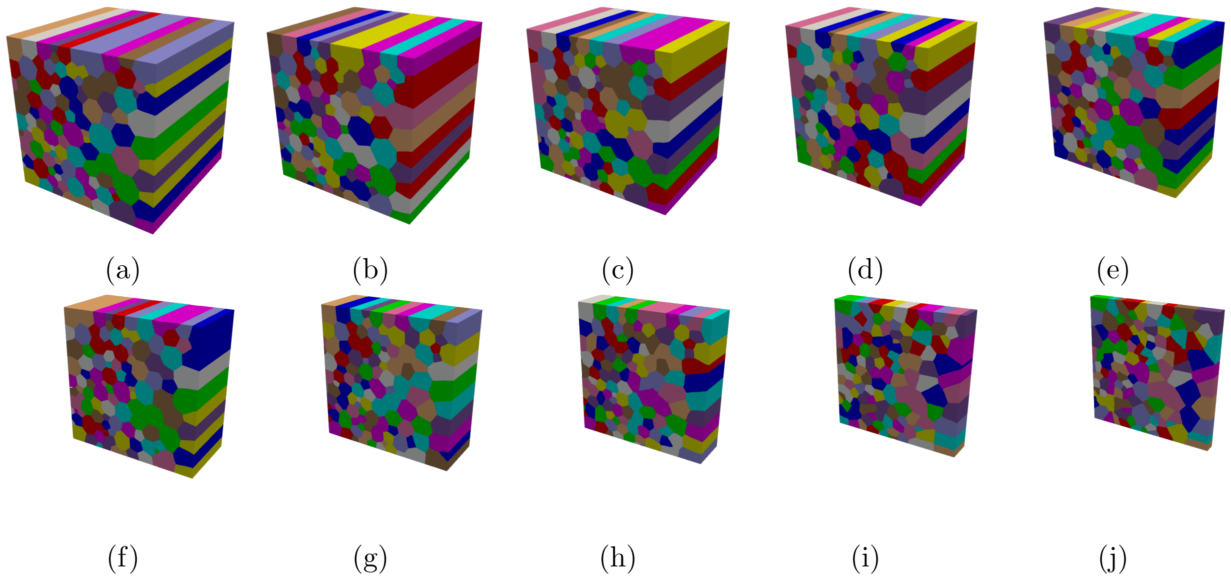

Figure 4.3: Columnar grained polycrystal with varying length along z with aspect ratio = (a) 0.083, (b) 0.091, (c) 0.101, (d) 0.12, (e) 0.136, (f) 0.173, (g) 0.205, (h) 0.281, (i) 0.415, and (j) 0.811

As before, the microstructures were generated using Neper where the length along z is varied (see Fig. 4.3). The aspect ratio is the ratio of the diameter of the grain and the length along z, where the average diameter is calculated using the line intercept method along x. These polycrystals are loaded along z with displacement along x, y, and z fixed at $x = 0$, $y = 0$, and $z = 0$, respectively. The creep response (Fig. 4.4) shows that the microstructrure with the highest aspect ratio (i.e. least width along z, Fig. 4.3(j)) has the least creep life. The creep life seems to be increasing as the length of the grains along the loading direction increases. Further investigation is being pursued in this direction where periodic microstructures are being considered for this case study in order to remove any edge-effects and look at a aggregate behavior of the material as result of this microstructure.

4.1.2 Modeling creep in realistic AM microstructures

The synthetic microstructures described in the previous subsection demonstrate how the grain morphology can influence the creep behavior. Next, we consider a representative AM microstructure to see how these factors influence the anisotropy in creep deformation in a more realistic structure.

An FE mesh for the microstructure is generated using voxelated data of a simulated AM microstructure [1], typical of AM stainless steel microstructures (but not a direct simulation of 316H). The meshing tool Sculpt was used to defeature the input data (64M data points, 10K grains) and create a manageable mesh with ∼440 grains meshed with 250K hexahedral elements (Fig. 4.5).

Assigning a single, constant orientation to each grain eliminates the orientation gradients found in the original structure. This may result a deformation behavior similar to a columnar

---

[1] Courtesy of Matt Rolchigo and Alex Plotkowski, ORNL

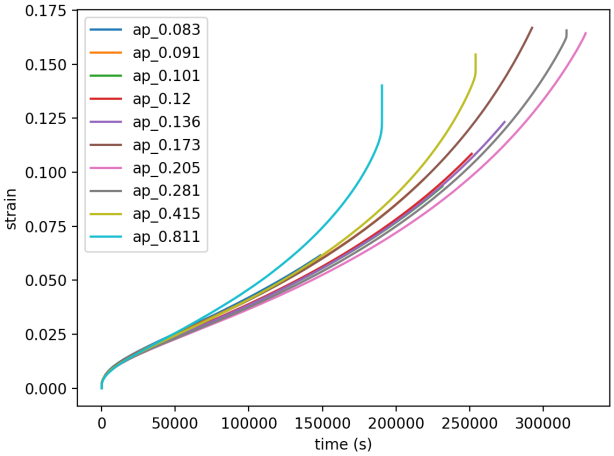

Figure 4.4: Creep comparison in columnar grained polycrystals with varying aspect ratio.

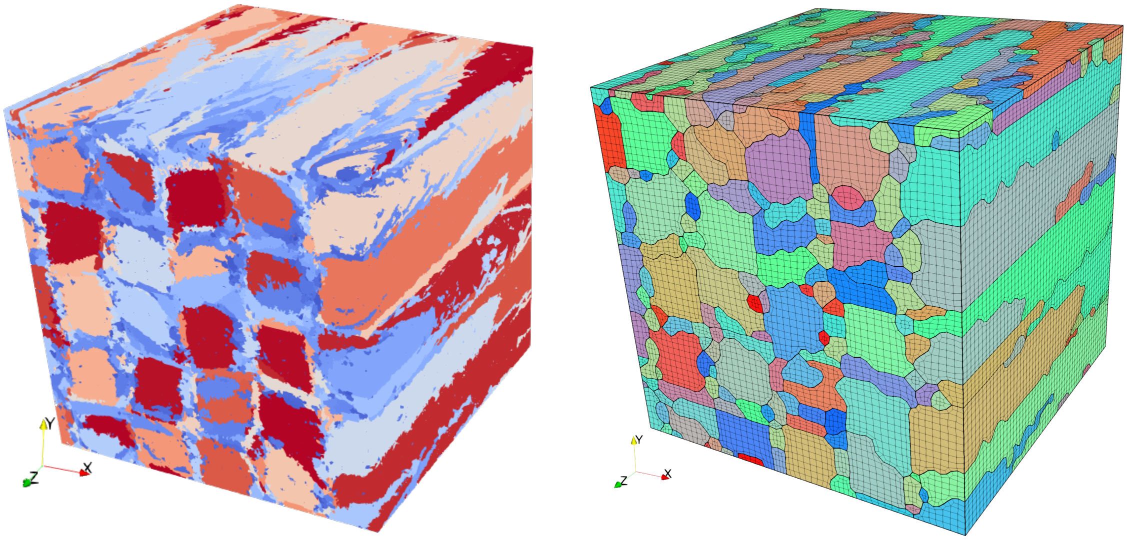

(a)

(b)

Figure 4.5: (a) Original voxelated data showing grain IDs at each grid point, (b) FE mesh created from the voxelated data

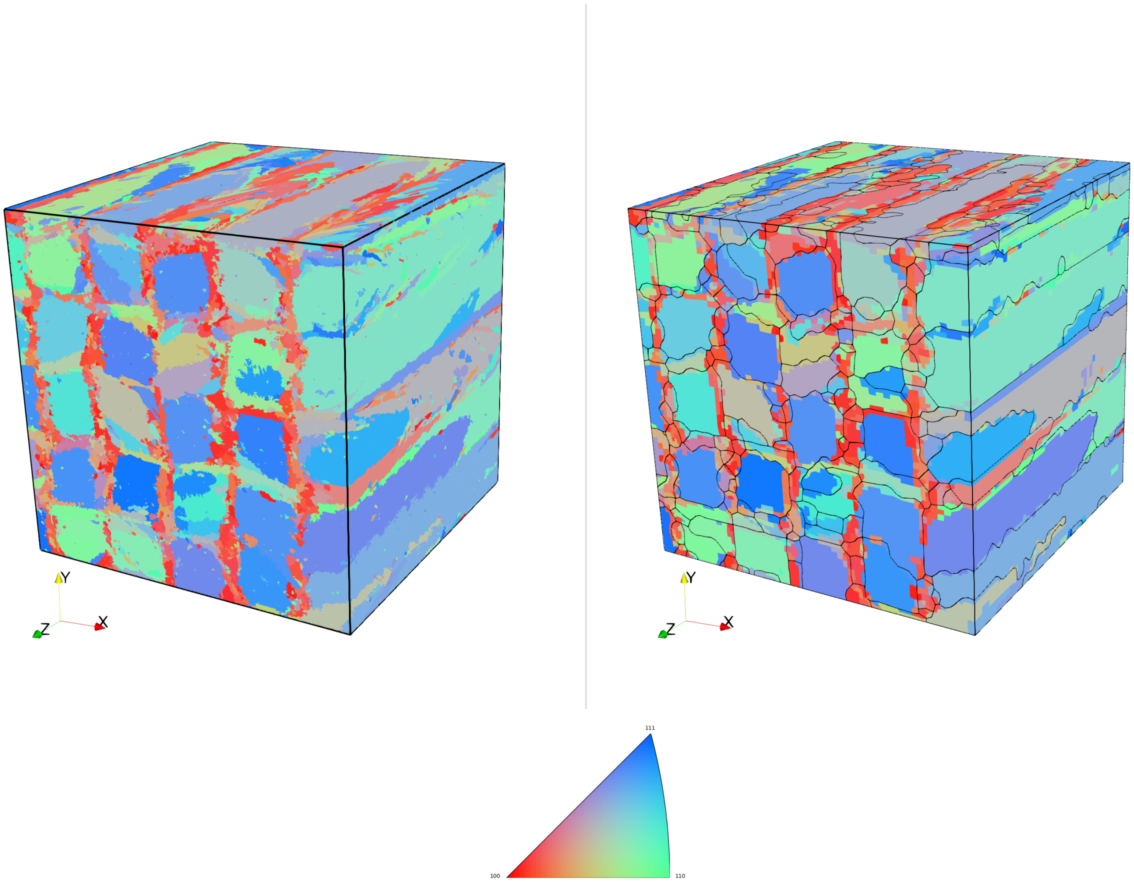

Figure 4.6: IPF color map of *Left:* Original data, and *Right:* FE mesh.

grained microstructure, with singular orientation through the length of the polycrystal, where the deformation of each grain will depend on its orientation (and thus the orientation of its slip systems) with respect to the loading direction and the build direction. This may make some grains more susceptible to plastic deformation and the resulting deformation is expected to be microstructure specific. In order to model a more general behavior of the microstructure we need to capture the orientation gradient in the polycrystal. To achieve this, we check all the grid points in the original data that lie inside a given element. Then the element is assigned an orientation matching the mode of the contained voxels. This way each element is assigned a unique orientation, rather than each grain having a uniform orientation. Fig. 4.6 compares the orientation in the original data and the orientation as mapped to the FE mesh.

The microstructure is then subjected to similar loading conditions as previous cases and as expected, the longer grains (along z) do result in a higher creep life. However, the results deviates from the experimental results in literature, such as that in [39, 40], in that they do not capture any creep cavitation mechanisms that might affect the creep strength. This is owing to the fact that the CPFEM model used here does not treat grain boundaries any differently than rest of the mesh. As a result this deformation behavior is expected - where deformation along the direction that does not provide barrier to slip and provides longer

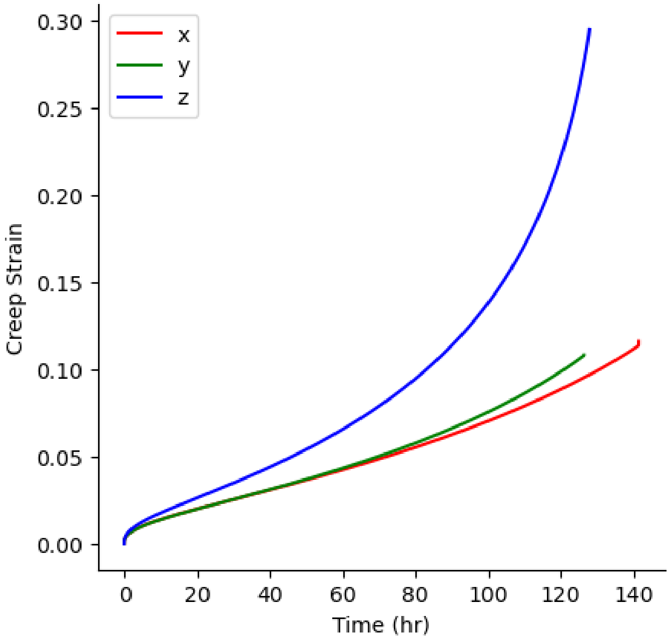

Figure 4.7: Simulated creep curve for AM microstructure

path for dislocation glide will result in larger plastic strain.

In order to capture the higher slip rate along the transverse directions (x and y), we need to incorporate a grain boundary cavitation model that allows diffusion along the grain boundaries as a result of the creep and allows void formation and growth. This may help us model the higher creep rate, as reported by Williams et al. [40]

4.1.3 Future work

Additional work is being pursued to understand the relationship between the aspect ratio of grains and the creep rate, where periodic microstructures are being used to understand if there is a clear trend in the creep behavior.

A grain boundary cavitation model is under investigation to accurately capture the creep rate along the transverse directions. Once implemented, finally, a physics based model for the creep deformation of 316H stainless steel developed by Hu and Kocks [43] will be used to accurately model the creep behavior of LPBF 316H.

4.2 The effect of dislocation structure on long-term strength

One of the significant characteristics of additively manufactured 316 stainless steel (AM 316 SS) is a cell dislocation structure of tangled dislocations, illustrated in Figure 4.8. This structure develops during the LPBF process as a result of the fast cooling rate. The structure has been demonstrated to have significant impact on mechanical properties, particularly when comparing AM materials to wrought or cast equivalents [44, 45, 46].

Numerous studies have been undertaken to understand the fundamental deformation mechanisms in AM 316, including both experimental [47, 48, 49, 50] and computational [51,

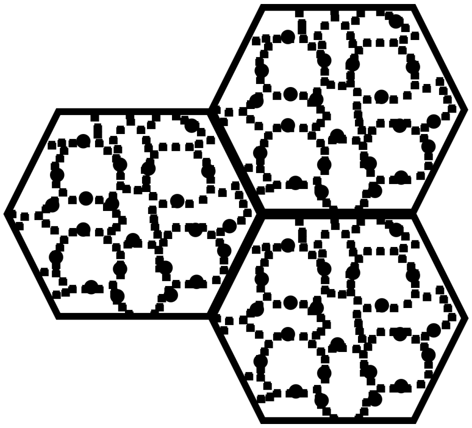

Figure 4.8: Schematic of the cell structure consisting of tangled dislocation.

52, 53, 54, 55] approaches. However, only few studies [56, 57] focus on the the performance of AM 316 SS subjected to long-term service at high temperatures. In this section, we propose a dislocation density based constitutive model for AM 316 materials which considers long-term thermal aging. The details of the development of the model are described here.

This model focuses only on the effect of the cell structure on dislocation hardening and thermal recovery. A complete model would have to account for precipitation hardening and recovery, including the effect of the dislocation cell structure on these mechanisms.

The resistance to slip contributed by the cell structure is the sum of slip resistance from both the cell wall and cell interiors

$$\tau_{crss} = \alpha_i G b \sqrt{\rho_i}(1 - f(1 - sf(d))) + \alpha_w G b \sqrt{\rho_w} f(1 - sf(d)) \tag{4.1}$$

where $sf(d)$ is a sigmoid function of wall size d, describing the influence of the existing cell structure satisfying certain critical wall size d_c requirement:

$$sf(d) = \frac{1}{1 + e^{-c(\frac{d}{d_c} - 1)}} \tag{4.2}$$

where d_c is critical wall size above which the effect of the pseudo Hall-Petch effect induced from the cell structure is diminished.

Further, the evolution of the cell structure has been demonstrated to be influenced by thermal recovery. For example, see Figure 4.9, where clear changes in the cell structure can be observed during the thermal aging period. We propose to account for thermal recovery with a simple Arrhenius-type model to evolve the cell size:

$$\dot{d} = k_0 e^{\frac{-Q}{RT}} d e^{\frac{-d}{d_c}} \tag{4.3}$$

Based on the experiments, the temperature not only affects the cell size, as reflected by Eq. 4.3, but also it also impacts the the thickness of the cell structure. To be specific, in experiment it has been observed that the cell wall size is relatively stable for temperatures cooler than $550°C$. Here, only the dislocation density in the cell wall has changed. To

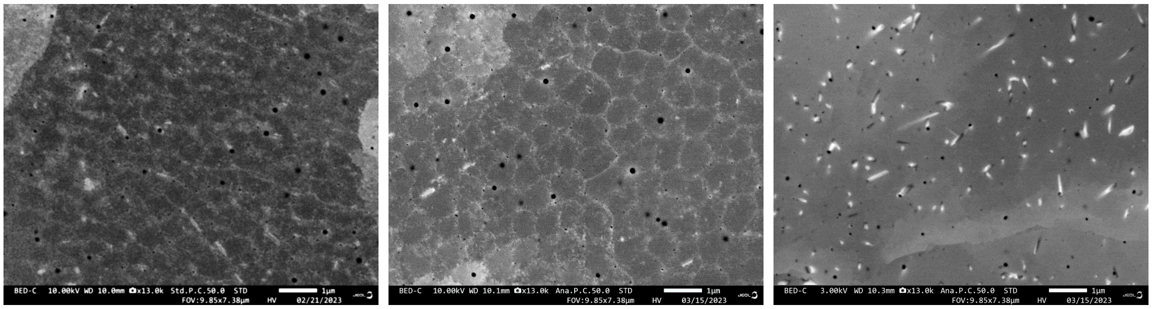

(a) as-built (b) $550°C - 500h$ (c) $750°C - 500h$

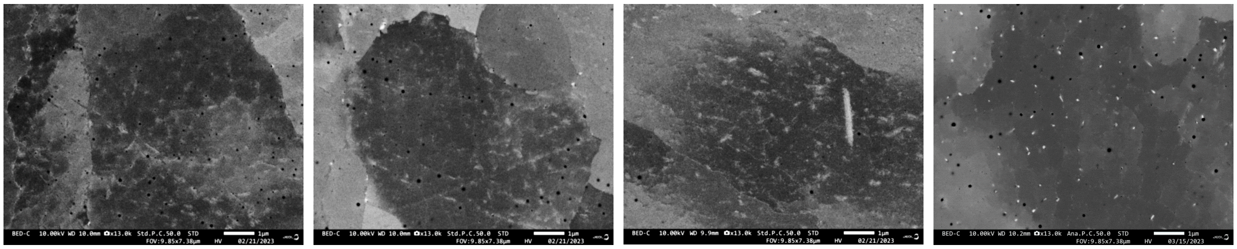

(d) $650°C - 5h$ (e) $650°C - 25h$ (f) $650°C - 100h$ (g) $650°C - 500h$

Figure 4.9: The influence of thermal aging on the microstructure of AM 316 SS under different period and temperature levels. Images provided by Xuan Zhang of Argonne National Laboratory.

account for this effect, we proposed a temperature dependent function to evaluate the volume fraction of cell structure based on the current cell size to represent the temperature dependent geometrical relationship between cell size and cell volume fraction as:

$$f = \frac{\mu\omega b^3}{kT}\frac{1}{d} + f_b \tag{4.4}$$

where $\omega = 1.687 \times 10^{-4}$ is the prefactor and f_b is the intercept accounting for the nonlinear geometric relationship. The rate form of the volume fraction of cell structure can then be obtained with:

$$\dot{f} = \frac{-kT}{\mu\omega b^3} f^2 d \tag{4.5}$$

We translate the cell and wall size to a slip resistance following a quasi-Hall-Petch relationship [58]. For example, Li *et al.* determined the quasi-Hall-Petch relation by measuring the resolved shear yield strength obtained from micro-pillars tests versus the cell structure size. Therefore, here we assume the dislocation density in the cell wall is dependent on the history of cell structure size:

$$d = \lambda < \rho_w >^{-0.5} \tag{4.6}$$

and its ODE form:

$$\dot{\rho_w} = (k_{w,1}\sqrt{< \rho_w >} - k_{w,2}(T) < \rho_w >)\dot{\gamma} + \frac{-2}{\lambda} < \rho_w >^{1.5} \dot{d}\frac{T}{T + T_r} f_{tr} \tag{4.7}$$

b	$k_{w,1}$	$k_{w,2}$	d_c	λ	α_w	α_i	c	E
0.256×10^{-9}	1.13×10^{9}	50.0	1.0×10^{-6}	1.0	0.95	0.25	1000.0	100000.0
m	$\dot{\varepsilon_0}$	d_0	Q	R	k_0	σ_{max}	σ_{rate}	f_0
0.01	1×10^{-4}	550×10^{-9}	1.0×10^{4}	8.3145	1.0×10^{-6}	20.0	1.0	0.25
$k_{i,1}$	$k_{i,2}$	x	g	D_0	$\dot{\varepsilon}_0$			
1.13×10^{8}	50.0	0.3	0.002	100.0	1.0×10^{3}			

Table 4.1: Model parameters.

and the evolution of the dislocation density in cell interior follows the traditional forest hardening model:

$$\dot{\rho}_i = (k_{i,1}\sqrt{< \rho_i >} - k_{i,2}(T) < \rho_i >)\dot{\gamma} + \frac{2}{\lambda} < \rho_w >^{1.5} \dot{d}\frac{T}{T+T_r} f_{tr} \tag{4.8}$$

where $k_{w,2}(T)$ is described as:

$$k_2(T) = xbgk_1(1 - \frac{kT}{D_0 b^3}) \ln \frac{\dot{\varepsilon}}{\dot{\varepsilon}_0} \tag{4.9}$$

$f_{tr} = 0.1$ represents the thermal recovery from the cell wall into the cell interior due to the change of the mobility of dislocation. x, g, D_0 are the coefficients of the recovery term and $\dot{\varepsilon}_0 = 1.0 \times 10^3$.

The calibrated model parameters are listed in Table 4.1.

With this model, the internal variables will be ρ_w, ρ_i, d and the system of ODEs are summarized in Algorithm 1. We implemented the constitutive model in *neml* — an open source material model library — into a standard single crystal, crystal plasticity, kinematic framework. *neml* provides basic crystal plasticity material models through both the integration of ODEs within *neml* internally and finite element solver externally. The Jacobians of the model with respect to the internal variables are also derived here.

Algorithm 1 The ODEs of the AM 316 model.

```
$\dot{d} = k_0 e^{\frac{-Q}{RT}} d e^{\frac{-d}{d_c}}$
$f = \frac{\mu \omega b^3}{kT} \frac{1}{d} \leftarrow d$
$sf(d) = \frac{1}{1+e^{-c(\frac{d}{d_c}-1)}} \leftarrow d$
$\dot{\rho_w} = (k_{w,1}\sqrt{< \rho_w >} - k_{w,2}(T) < \rho_w >)\dot{\gamma} + \frac{-2}{\lambda} < \rho_w >^{1.5} \dot{d}\frac{T}{T+T_r} f_{tr}$
$\dot{\rho_i} = (k_{i,1}\sqrt{< \rho_i >} - k_{i,2}(T) < \rho_i >)\dot{\gamma} + \frac{2}{\lambda} < \rho_w >^{1.5} \dot{d}\frac{T}{T+T_r} f_{tr}$
$\tau_{crss} = \alpha_i G b \sqrt{\rho_i}(1 - f(1 - sf(d))) + \alpha_w G b \sqrt{\rho_w} f(1 - sf(d)) \leftarrow \rho_i, \rho_w, d$
```

$\dot{h}$ are:

$$\dot{h} = \begin{bmatrix} k_0 e^{\frac{-Q}{RT}} d e^{\frac{-d}{d_c}} \\ (k_{w,1}\sqrt{<\rho_w>} - k_{w,2}(T) <\rho_w>)\dot{\gamma} + \frac{-2}{\lambda} <\rho_w>^{1.5}\ \dot{d}\frac{T}{T+T_r} f_{tr} \\ \vdots \\ (k_{i,1}\sqrt{<\rho_i>} - k_{i,2}(T) <\rho_i>)\dot{\gamma} + \frac{2}{\lambda} <\rho_w>^{1.5}\ \dot{d}\frac{T}{T+T_r} f_{tr} \\ \vdots \end{bmatrix} \tag{4.10}$$

τ are:

$$\tau = \begin{bmatrix} \alpha_i G b\sqrt{<\rho_i>}(1 - f(1 - sf(d))) + \alpha_w G b\sqrt{<\rho_w>} f(1 - sf(d)) \\ \vdots \end{bmatrix} \tag{4.11}$$

$\frac{dh}{d\tau}$ are:

$$\frac{df}{dd} = \frac{-\mu\omega b^3}{kT} d^{-2}$$

$$\frac{dsf}{dd} = \frac{c}{d_c} e^{-c(\frac{d}{d_c}-1)}(1 + e^{-c(\frac{d}{d_c}-1)})^{-2}$$

$$\frac{d\tau}{dh} = \begin{bmatrix} \alpha_i G b\sqrt{<\rho_i>}(-\frac{df}{dd} + \frac{df}{dd} sf + f\frac{dsf}{dd}) + \alpha_w G b\sqrt{<\rho_w>}(\frac{df}{dd} - (\frac{df}{dd} sf + f\frac{dsf}{dd})) \\ \vdots \\ \frac{1}{2}\alpha_w G b <\rho_w>^{\frac{-1}{2}}\ f(1 - sf) \\ \vdots \\ \frac{1}{2}\alpha_i G b <\rho_i>^{\frac{-1}{2}}\ (1 - f(1 - sf)) \\ \vdots \end{bmatrix} \tag{4.12}$$

$\frac{d\dot{h}}{d\sigma}$ are:

$$\frac{d\dot{h}}{d\sigma} = \begin{bmatrix} 0 \\ \vdots \\ (k_{w,1}\sqrt{<\rho_w>} - k_{w,2}(T) <\rho_w>)\frac{\dot{\gamma}}{d\sigma} \\ \vdots \\ (k_{i,1}\sqrt{<\rho_i>} - k_{i,2}(T) <\rho_i>)\frac{\dot{\gamma}}{d\sigma} \\ \vdots \end{bmatrix} \tag{4.13}$$

$\frac{d\dot{h}}{dh}$ are:

$$\begin{cases} \frac{\partial \dot{d}}{\partial d} = k_0 e^{\frac{-Q}{RT}} e^{\frac{-d}{d_c}}(1 - \frac{d}{d_c}), & \text{if } self \\ 0, & \text{otherwise} \end{cases}$$

$$\frac{\partial \dot{d}}{\partial \rho_w} = 0.0$$

$$\frac{\partial \dot{d}}{\partial \rho_i} = 0.0$$

$$\frac{\partial \dot{\rho_w}}{\partial d} = (k_{w,1}\sqrt{<\rho_w>} - k_{w,2}(T) < \rho_w >)\frac{\partial \dot{\gamma}}{\partial d} - \frac{2}{\lambda} < \rho_w^{1.5} > k_0 e^{\frac{-Q}{RT}} \frac{T}{T+T_r} f_{tr} e^{\frac{-d}{d_c}} (1 - \frac{d}{d_c})$$

$$\frac{\partial \dot{\rho_w}}{\partial \rho_w} = \begin{cases} (\frac{1}{2}k_{w,1} < \rho_w >^{\frac{-1}{2}} - k_{w,2})\dot{\gamma} - \frac{3}{\lambda} < \rho_w >^{0.5} \dot{d}\frac{T}{T+T_r} f_{tr}, & \text{if } self \\ (k_{w,1}\sqrt{<\rho_w>} - k_{w,2} < \rho_w >)\frac{\partial \dot{\gamma}}{\partial \rho_w}, & \text{otherwise} \end{cases}$$

$$\frac{\partial \dot{\rho_w}}{\partial \rho_i} = (k_{w,1}\sqrt{<\rho_w>} - k_{w,2}(T) < \rho_w >)\frac{\partial \dot{\gamma}}{\partial \rho_i}$$

$$\frac{\partial \dot{\rho_i}}{\partial d} = (k_{i,1}\sqrt{<\rho_i>} - k_{i,2}(T) < \rho_i >)\frac{\partial \dot{\gamma}}{\partial d} + \frac{2}{\lambda} < \rho_w^{1.5} > k_0 e^{\frac{-Q}{RT}} \frac{T}{T+T_r} f_{tr} e^{\frac{-d}{d_c}} (1 - \frac{d}{d_c})$$

$$\frac{\partial \dot{\rho_i}}{\partial \rho_w} = \begin{cases} \frac{3}{\lambda} < \rho_w^{0.5} > \dot{d}\frac{T}{T+T_r} f_{tr}, & \text{if } self + 12 \\ (k_{i,1}\sqrt{<\rho_i>} - k_{i,2}(T) < \rho_i >)\frac{\partial \dot{\gamma}}{\partial \rho_w}, & \text{otherwise} \end{cases}$$

$$\frac{\partial \dot{\rho_i}}{\partial \rho_i} = \begin{cases} (\frac{1}{2}k_{i,1} < \rho_i >^{\frac{-1}{2}} - k_{i,2})\dot{\gamma}, & \text{if } self \\ (k_{i,1}\sqrt{<\rho_i>} - k_{i,2} < \rho_i >)\frac{\partial \dot{\gamma}}{\partial \rho_i}, & \text{otherwise} \end{cases}$$

$$\frac{d\dot{h}}{dh} = \begin{bmatrix} [\frac{\partial \dot{d}}{d}] \times 1 + [\frac{\partial \dot{d}}{\rho_w}] \times 12 + [\frac{\partial \dot{d}}{\rho_i}] \times 12 \\ \vdots \\ [\frac{\partial \dot{\rho_w}}{d}] \times 1 + [\frac{\partial \dot{\rho_w}}{\rho_w}] \times 12 + [\frac{\partial \dot{\rho_w}}{\rho_i}] \times 12 \\ \vdots \\ [\frac{\partial \dot{\rho_i}}{d}] \times 1 + [\frac{\partial \dot{\rho_i}}{\rho_w}] \times 12 + [\frac{\partial \dot{\rho_i}}{\rho_i}] \times 12 \\ \vdots \end{bmatrix} \tag{4.14}$$

$\frac{d\dot{h}}{d_{ext}}$ are:

$$\frac{d\dot{h}}{d_{ext}} = \begin{bmatrix} 0 \\ \vdots \\ (k_{w,1}\sqrt{<\rho_w>} - k_{w,2}(T) < \rho_w >)\frac{\partial \dot{\gamma}}{\partial h} \\ \vdots \\ (k_{i,1}\sqrt{<\rho_i>} - k_{i,2}(T) < \rho_i >)\frac{\partial \dot{\gamma}}{\partial h} \\ \vdots \end{bmatrix} \tag{4.15}$$

Figure 4.10 displays the predicted thermal aging results vs. the actual measurement from the experiments at 650° C. Figure 4.11 plots the predicted stress-strain curves vs. the actual result for the aged uniaxial tension tests.

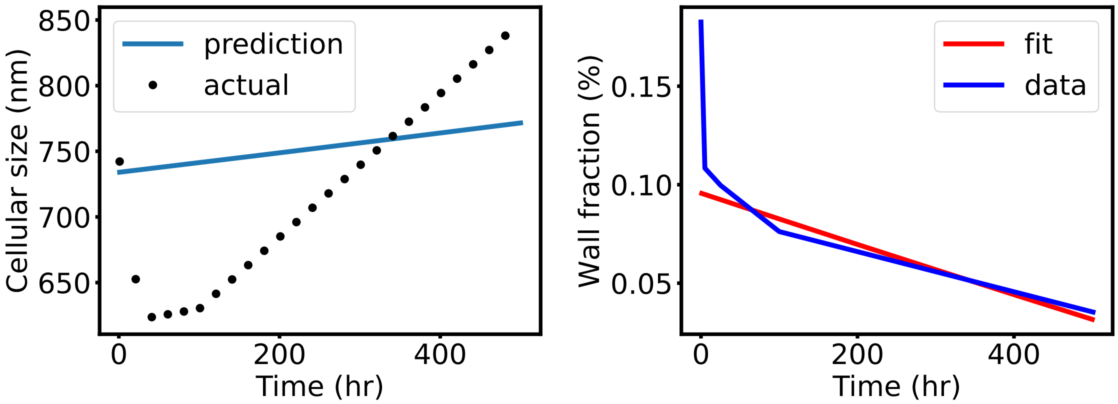

(a) Cell size

(b) Cell volume fraction

Figure 4.10: (a) Predicted cell wall size vs. the actual experiment measurements. (b) Predicted cell volume fraction vs. the actual experiment measurements during thermal aging process at 650°C.

The model adequately captures the change in the material flow stress with time-at-temperature. Similarly, it reasonably captures the cell volume fraction from the experiments. It does not capture the complex evolution in cell size (recovery followed by growth), but rather models only a uniform growth rate with temperature.

Future work might improve these model predictions by improving the cell growth kinematics. Additionally, we might extend these predictions to longer aging times and higher temperatures. As noted above, a complete model would also need to account for precipitation kinetics in the material, in particular the interaction between precipitation and the cell structure.

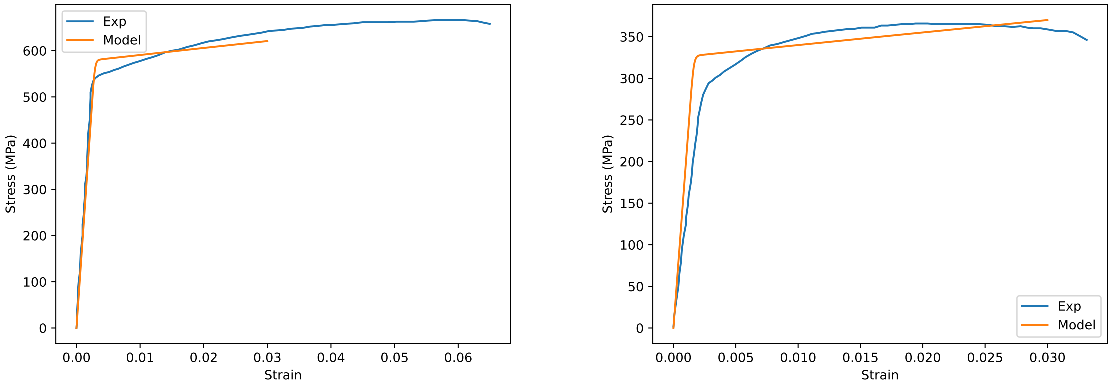

(a) as-built

(b) $650°C - 5h$

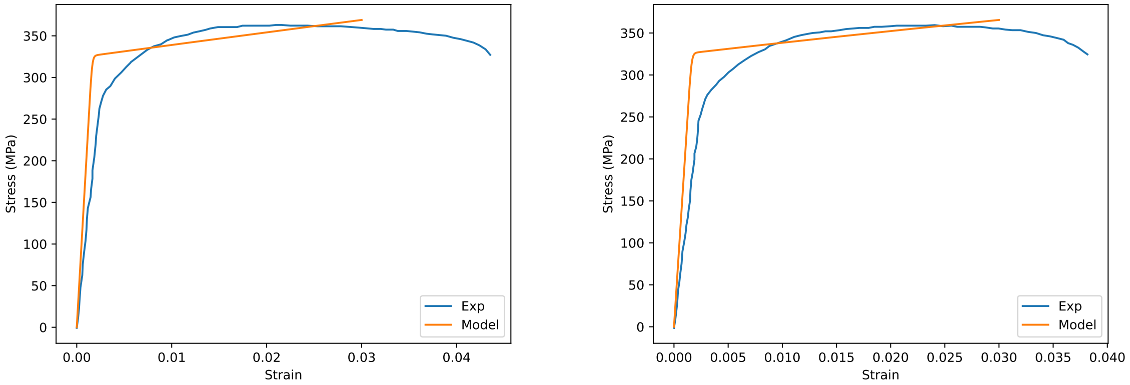

(c) $650°C - 25h$

(d) $650°C - 100h$

Figure 4.11: Predicted stress-strain curves vs. experimental aged uniaxial tension tests starting from different thermal aging period (a) as-built; (b) 5h under $650°C$; (c) 25h under $650°C$; (d) 100h under $650°C$;.

5 Conclusions

This report summarizes preliminary models to understand and predict key mechanisms contributing to the long-term strength of LPBF 316H stainless steel. Specifically, the report details models for:

1. radiation creep and void swelling
2. the influence of local internal stress on the precipitation of second phases
3. the effect of AM-specific grain and dislocation cell structure.

All of these mechanisms will have an influence on the long-term strength of the LPBF material. These models focus, in particular, on aspects of the LPBF microstructure that differ from wrought materials, with the goal of improving our understanding of the underlying mechanisms and making better, more accurate long-term predictions for material strength.

Already this report makes some preliminary long-term predictions for the behavior of LPBF 316H under creep and thermal aging conditions. However, additional work will be required to improve these mechanism models, and, especially, to integrate the models into a unified framework for simulating the response of LPBF materials. Such a unified model will need to account for interactions between the individual mechanisms. Two examples of such interactions might be:

- The local internal stress caused by the dislocation cell structure provides a localized driving force for precipitation (in addition to chemical segregation). This will cause precipitates to prefer cell walls as favorable nucleation sites imprinting the dislocation structure on the subsequent precipitation structure. This, in turn, will influence precipitation hardening and affect the material strength.
- The dislocation network might act as sinks for radiation-induced defects in the material microstructure, improving the resistance of the material to radiation damage.

This unified model could be developed and validated against short-term test data and microstructural observations of AM material. One main use of such a validated model would be to make predictions for the long-term material strength under representative high temperature reactor operating conditions. Currently, such predictions are often made with empirical models that may be inaccurate when extrapolating far outside the available experimental test durations. Physics-based models should have improved accuracy for making these long term predictions, which could reduce the number of duration of tests required to qualify LPBF 316H and future advanced materials.

Directly validating such a model is challenging as long-term data would be required. One approach might be to collect detailed data on a limited amount of material to serve as a challenge validation problem for the model. An example might be a creep test on a single sample coupled with detailed, pre-deformation characterization of the sample microstructure. Successfully predicting creep crack initiation and growth through the material structure would be a powerful validation example, even if the duration of the creep test does not cover full plant component design lives.

Acknowledgements

The work of the ANL authors was sponsored by the U.S. Department of Energy, under Contract No. DE-AC02-06CH11357 with Argonne National Laboratory, managed and operated by UChicago Argonne LLC. We gratefully acknowledge the computing resources provided on Bebop, a high-performance computing cluster operated by the Laboratory Computing Resource Center at Argonne National Laboratory.

For the INL authors, this work was prepared for the U.S. Department of Energy, Office of Nuclear Energy, under DOE Idaho Operations Office, Contract DE-AC07-05ID14517. Additionally portions of this research made use of the resources of the High Performance Computing Center at Idaho National Laboratory, which is supported by the Office of Nuclear Energy of the U.S. Department of Energy and the Nuclear Science User Facilities under Contract No. DE-AC07-05ID14517.

For the LANL authors, this research used resources provided by the Los Alamos National Laboratory Institutional Computing Program, which is supported by the U.S. Department of Energy National Nuclear Security Administration under Contract No. 89233218CNA000001.

The authors acknowledge support for this work from the Advanced Materials and Manufacturing Technologies (AMMT) program with programmatic guidance provided by Meimei Li at Argonne National Laboratory, David Andersson at Los Alamos National Laboratory, Ryan Dehoff at Oak Ridge National Laboratory and Dirk Cairns-Gallimore at the Department of Energy.

We thank Xuan Zhang of Argonne National Laboratory for providing the thermal aging data on LPBF 316H.

Bibliography

[1] C. Cawthorne and E. Fulton, "Voids in irradiated stainless steel," Nature, vol. 216, pp. 575–576, 11 1967.

[2] G. S. Was and S. Ukai, "Chapter 8 - austenitic stainless steels," in Structural Alloys for Nuclear Energy Applications (G. R. Odette and S. J. Zinkle, eds.), pp. 293–347, Boston: Elsevier, 1 2019.

[3] J. Gittus, "Theory of dislocation-creep due to the frenkel defects or interstitialcies produced by bombardment with energetic particles," The Philosophical Magazine: A Journal of Theoretical Experimental and Applied Physics, vol. 25, no. 2, pp. 345–354, 1972.

[4] S. J. Zinkle, H. Tanigawa, and B. D. Wirth, "Chapter 5 - radiation and thermomechanical degradation effects in reactor structural alloys," in Structural Alloys for Nuclear Energy Applications (G. R. Odette and S. J. Zinkle, eds.), pp. 163–210, Boston: Elsevier, 2019.

[5] G. S. Was, Chapter 14 - Irradiation Creep and Growth, pp. 711–763. Berlin: Springer-Verlag, 1 2007.

[6] A. Fissolo, R. Cauvin, J.-P. Hugot, and V. Levy, "Influence of swelling on irradiated cw titanium modified 316 embrittlement," in Effects of Radiation on Materials: 14th International Symposium, Volume II (N. Packan, R. Stoller, and A. Kumar, eds.), pp. 700–713, Philadelphia: ASTM, 1 1990.

[7] Idaho National Laboratory, "Compute multiple crystal plasticity stress, MOOSE documentation," 2021. `https://mooseframework.inl.gov/source/materials/crystal\_plasticity/ComputeMultipleCrystalPlasticityStress.html`, Last accessed on 2023-08-01.

[8] S. R. Kalidindi, "Modeling anisotropic strain hardening and deformation textures in low stacking fault energy fcc metals," International Journal of Plasticity, vol. 17, pp. 837–860, 2001.

[9] P. Chakraborty and S. B. Biner, "Crystal plasticity modeling of irradiation effects on flow stress in pure-iron and iron-copper alloys," Mechanics of Materials, vol. 101, pp. 71–80, 2016.

[10] S. A. Pitts, W. Jiang, D. Pizzocri, E. I. Barker, and H. M. Zbib, "A continuum dislocation dynamics crystal plasticity approach to irradiated body-centered cubic α-iron," Journal of Engineering Materials and Technology, vol. 144, 1 2022.

[11] D. Hull and D. Bacon, "Chapter 3 - movement of dislocations," in Introduction to Dislocations (Fifth Edition) (D. Hull and D. Bacon, eds.), pp. 43–62, Oxford: Butterworth-Heinemann, fifth edition ed., 2011.

[12] A. Patra and D. L. McDowell, "Crystal plasticity investigation of the microstructural factors influencing dislocation channeling in a model irradiated bcc material," Acta Materialia, vol. 110, pp. 364–376, 2016.

[13] "MOOSE GitHub repository," 2023. `https://github.com/idaholab/moose`, Last accessed on 2023-08-02.

[14] J. Hu and A. C. Cocks, "A multi-scale self-consistent model describing the lattice deformation in austenitic stainless steels," International Journal of Solids and Structures, vol. 78-79, pp. 21–37, 1 2016.

[15] A. Patra and D. L. McDowell, "Crystal plasticity-based constitutive modelling of irradiated bcc structures," Philosophical Magazine, vol. 92, pp. 861–887, 3 2012.

[16] D. Li, H. Zbib, X. Sun, and M. Khaleel, "Predicting plastic flow and irradiation hardening of iron single crystal with mechanism-based continuum dislocation dynamics," International Journal of Plasticity, vol. 52, pp. 3–17, 2014.

[17] W. Wen, A. Kohnert, M. A. Kumar, L. Capolungo, and C. N. Tomé, "Mechanism-based modeling of thermal and irradiation creep behavior: An application to ferritic/martensitic ht9 steel," International Journal of Plasticity, vol. 126, 3 2020.

[18] J. Hu, B. Chen, D. J. Smith, P. E. Flewitt, and A. C. Cocks, "On the evaluation of the bauschinger effect in an austenitic stainless steel—the role of multi-scale residual stresses," International Journal of Plasticity, vol. 84, pp. 203–223, 9 2016.

[19] G. S. Was, Chapter 8 - Irradiation-Induced Voids and Bubbles, pp. 343–432. Berlin: Springer-Verlag, 1 2007.

[20] F. Meissonnier, E. Busso, and N. O'Dowd, "Finite element implementation of a generalised non-local rate-dependent crystallographic formulation for finite strains," International Journal of Plasticity, vol. 17, no. 4, pp. 601–640, 2001.

[21] Idaho National Laboratory, "Compute crystal plasticity thermal eigenstrain, MOOSE documentation," 2021. `https://mooseframework.inl.gov/source/materials/crystal\_plasticity/ComputeCrystalPlasticityThermalEigenstrain.html`, Last accessed on 2023-08-01.

[22] J. Li, I. Romero, and J. Segurado, "Development of a thermo-mechanically coupled crystal plasticity modeling framework: application to polycrystalline homogenization," International Journal of Plasticity, vol. 119, pp. 313–330, 2019.

[23] M. Rieth, "A comprising steady-state creep model for the austenitic AISI 316 L(N) steel," Journal of Nuclear Materials, vol. 367-370, pp. 915–919, 8 2007.

[24] J. Matthews and M. Finnis, "Irradiation creep models—an overview," Journal of Nuclear Materials, vol. 159, pp. 257–285, 1988.

[25] J. Hu and A. Cocks, "Effect of creep on the bauschinger effect in a polycrystalline austenitic stainless steel," Scripta Materialia, vol. 128, pp. 100–104, 2 2017.

[26] J. Hu, G. Green, S. Hogg, R. Higginson, and A. Cocks, "Effect of microstructure evolution on the creep properties of a polycrystalline 316h austenitic stainless steel," Materials Science and Engineering: A, vol. 772, p. 138787, 1 2020.

[27] Y. M. Wang, T. Voisin, J. T. McKeown, J. Ye, N. P. Calta, Z. Li, Z. Zeng, Y. Zhang, W. Chen, T. T. Roehling, R. T. Ott, M. K. Santala, P. J. Depond, M. J. Matthews, A. V. Hamza, and T. Zhu, "Additively manufactured hierarchical stainless steels with high strength and ductility," Nature Materials, vol. 17, no. 1, pp. 63–71, 2018.

[28] C. Bronkhorst, J. Mayeur, V. Livescu, R. Pokharel, D. Brown, and G. Gray, "Structural representation of additively manufactured 316l austenitic stainless steel," International Journal of Plasticity, vol. 118, pp. 70–86, 2019.

[29] K. Bertsch, G. Meric de Bellefon, B. Kuehl, and D. Thoma, "Origin of dislocation structures in an additively manufactured austenitic stainless steel 316l," Acta Materialia, vol. 199, pp. 19–33, 2020.

[30] Z. Sheng, M. Bonvalet Rolland, T. Zhou, J. Odqvist, and P. Hedström, "Langer–schwartz–kampmann–wagner precipitation simulations: assessment of models and materials design application for cu precipitation in ph stainless steels," Journal of Materials Science, vol. 56, no. 3, pp. 2650–2671, 2021.

[31] S. Ryu and W. Cai, "Validity of classical nucleation theory for ising models," Phys. Rev. E, vol. 81, p. 030601, Mar 2010.

[32] A. Dinsdale, "SGTE data for pure elements," Calphad, vol. 15, no. 4, pp. 317–425, 1991.

[33] E. Polatidis, G. Haidemenopoulos, D. Krizan, N. Aravas, T. Panzner, M. Šmíd, I. Papadioti, N. Casati, S. Van Petegem, and H. Van Swygenhoven, "The effect of stress triaxiality on the phase transformation in transformation induced plasticity steels: Experimental investigation and modelling the transformation kinetics," Materials Science and Engineering: A, vol. 800, p. 140321, 2021.

[34] J. Svoboda, F. Fischer, P. Fratzl, and E. Kozeschnik, "Modelling of kinetics in multicomponent multi-phase systems with spherical precipitates: I: Theory," Materials Science and Engineering: A, vol. 385, no. 1, pp. 166–174, 2004.

[35] T. Mura, Micromechanics of defects in solids, vol. 3 of Mechanics of Elastic and Inelastic Solids. Dordrecht: Springer Netherlands, 1987.

[36] P. Voorhees and W. C. Johnson, "The thermodynamics of elastically stressed crystals," in Solid State Physics (H. Ehrenreich and F. Spaepen, eds.), vol. 59, pp. 1–201, Academic Press, 2004.

[37] S. Eich, D. Beinke, and G. Schmitz, "Embedded-atom potential for an accurate thermodynamic description of the iron–chromium system," Computational Materials Science, vol. 104, pp. 185–192, 2015.

[38] S. Ghorbanpour, M. E. Alam, N. C. Ferreri, A. Kumar, B. A. McWilliams, S. C. Vogel, J. Bicknell, I. J. Beyerlein, and M. Knezevic, "Experimental characterization and crystal plasticity modeling of anisotropy, tension-compression asymmetry, and texture evolution of additively manufactured inconel 718 at room and elevated temperatures," International Journal of Plasticity, vol. 125, pp. 63–79, 2020.

[39] J. Shi, S. Zhou, H. Chen, G. Cao, A. Russell, Z. Zhou, X. Qi, C. Li, and G. Chen, "Microstructure and creep anisotropy of inconel 718 alloy processed by selective laser melting," Materials Science and Engineering: A, vol. 805, p. 140583, 2021.

[40] R. J. Williams, J. Al-Lami, P. A. Hooper, M.-S. Pham, and C. M. Davies, "Creep deformation and failure properties of 316 l stainless steel manufactured by laser powder bed fusion under multiaxial loading conditions," Additive Manufacturing, vol. 37, p. 101706, 2021.

[41] A. Venkataraman and M. C. Messner, "An initial framework for the rapid qualification of long-term creep rupture strength via microstructural modeling," Tech. Rep. ANL-21/34, Argonne National Laboratory, 2021.

[42] R. Quey and M. Kasemer, "The neper/fepx project: free/open-source polycrystal generation, deformation simulation, and post-processing," in IOP Conference Series: Materials Science and Engineering, vol. 1249, p. 012021, IOP Publishing, 2022.

[43] J. Hu, G. Green, S. Hogg, R. Higginson, and A. Cocks, "Effect of microstructure evolution on the creep properties of a polycrystalline 316h austenitic stainless steel," Materials Science and Engineering: A, vol. 772, p. 138787, 2020.

[44] L. Cui, S. Jiang, J. Xu, R. L. Peng, R. T. Mousavian, and J. Moverare, "Revealing relationships between microstructure and hardening nature of additively manufactured 316L stainless steel," Materials & Design, vol. 198, p. 109385, 2021.

[45] Y. Hong, C. Zhou, Y. Zheng, L. Zhang, and J. Zheng, "The cellular boundary with high density of dislocations governed the strengthening mechanism in selective laser melted 316l stainless steel," Materials Science and Engineering: A, vol. 799, p. 140279, 2021.

[46] L. Liu, Q. Ding, Y. Zhong, J. Zou, J. Wu, Y.-L. Chiu, J. Li, Z. Zhang, Q. Yu, and Z. Shen, "Dislocation network in additive manufactured steel breaks strength–ductility trade-off," Materials Today, vol. 21, no. 4, pp. 354–361, 2018.

[47] M. Shamsujjoha, S. R. Agnew, J. M. Fitz-Gerald, W. R. Moore, and T. A. Newman, "High strength and ductility of additively manufactured 316L stainless steel explained," Metallurgical and Materials Transactions A, vol. 49, pp. 3011–3027, 2018.

[48] Y. Zhong, L. Liu, S. Wikman, D. Cui, and Z. Shen, "Intragranular cellular segregation network structure strengthening 316L stainless steel prepared by selective laser melting," Journal of Nuclear Materials, vol. 470, pp. 170–178, 2016.

[49] X. Zhang, P. Kenesei, J.-S. Park, J. Almer, and M. Li, "In situ high-energy x-ray study of deformation mechanisms in additively manufactured 316l stainless steel," Journal of Nuclear Materials, vol. 549, p. 152874, 2021.

[50] Y. M. Wang, T. Voisin, J. T. McKeown, J. Ye, N. P. Calta, Z. Li, Z. Zeng, Y. Zhang, W. Chen, T. T. Roehling, et al., "Additively manufactured hierarchical stainless steels with high strength and ductility," Nature materials, vol. 17, no. 1, pp. 63–71, 2018.

[51] M. Lindroos, T. Pinomaa, A. Antikainen, J. Lagerbom, J. Reijonen, T. Lindroos, T. Andersson, and A. Laukkanen, "Micromechanical modeling approach to single track deformation, phase transformation and residual stress evolution during selective laser melting using crystal plasticity," Additive Manufacturing, vol. 38, p. 101819, 2021.

[52] M. Lindroos, T. Pinomaa, K. Ammar, A. Laukkanen, N. Provatas, and S. Forest, "Dislocation density in cellular rapid solidification using phase field modeling and crystal plasticity," International Journal of Plasticity, vol. 148, p. 103139, 2022.

[53] Y. Cao, Z. Moumni, J. Zhu, X. Gu, Y. Zhang, X. Zhai, and W. Zhang, "Effect of scanning speed on fatigue behavior of 316l stainless steel fabricated by laser powder bed fusion," Journal of Materials Processing Technology, p. 118043, 2023.

[54] A. S. Sabau, L. Yuan, J.-L. Fattebert, and J. A. Turner, "An OpenMP GPU-offload implementation of a non-equilibrium solidification cellular automata model for additive manufacturing," Computer Physics Communications, vol. 284, p. 108605, 2023.

[55] J. Kwon, G. Karthik, Y. Estrin, and H. S. Kim, "Constitutive modeling of cellular-structured metals produced by additive manufacturing," Acta Materialia, vol. 241, p. 118421, 2022.

[56] M. Li, X. Zhang, W.-Y. Chen, and T. S. Byun, "Creep behavior of 316L stainless steel manufactured by laser powder bed fusion," Journal of Nuclear Materials, vol. 548, p. 152847, 2021.

[57] M. Li, W.-Y. Chen, and X. Zhang, "Effect of heat treatment on creep behavior of 316 l stainless steel manufactured by laser powder bed fusion," Journal of Nuclear Materials, vol. 559, p. 153469, 2022.

[58] D. Kong, C. Dong, S. Wei, X. Ni, L. Zhang, R. Li, L. Wang, C. Man, and X. Li, "About metastable cellular structure in additively manufactured austenitic stainless steels," Additive Manufacturing, vol. 38, p. 101804, 2021.

Applied Materials Division
Argonne National Laboratory
9700 South Cass Avenue, Bldg. 212
Argonne, IL 60439

www.anl.gov

Argonne National Laboratory is a U.S. Department of Energy
laboratory managed by UChicago Argonne, LLC